UNIVERSIDADE TÉCNICA DE LISBOA

INSTITUTO SUPERIOR TÉCNICO

Structural and chemical diversity of sialoliths

Olga Isabel da Luísa e Santo

(Licenciada)

Dissertação para obtenção do Grau de Mestre em Ciência e Engenharia de Materiais

Orientador: Doutora Patrícia Maria Cristovam Cipriano Almeida de Carvalho

Co-Orientador: Doutor António Pedro Alves de Matos

Júri

Presidente: Doutora Maria Emília da Encarnação Rosa

Vogais: Doutor António Pedro Alves de Matos

Doutor Arlindo Pereira de Almeida

Doutor Luís Filipe da Silva dos Santos

Doutora Patrícia Maria Cristovam Cipriano Almeida de Carvalho

Outubro 2008

Se non è vero, è ben trovato

(Italian proverb)

Acknowledgments

I will never forget the day when my primary school teacher, D. Ana Maria, said to the boys and girls in the classroom that "water doesn't spring" and after what she explained the whole cycle of water. We were astonished! In that day I learned the difference and the value of both, poetic and scientific liberty! That lady is one of the persons responsible for this work, but she is not the only one. All the teachers and professors I had in the past and all that I have now are responsible for feeding the curiosity and the conviction that we can understand the world a little better. To all of them, thank you!

This modest work would not have been possible without the co-operation, assistance, patience, understanding and knowledge of several persons to which I am deeply grateful. I must thank Prof. Maria Emília Rosa for the clear and prompt reply to formal questions related to this work. I would like to thank Profs. Luís Santos, Rogério Colaço and Dr. Teresa Nunes for their support, technical assistance and help in results interpretation. I am also grateful to Dr. Isabel Nogueira for all the technical explanations and for the trust in my ability to use the laboratory equipment. I would like to thank Ph.D. students Daniela Nunes, Edson Santos and especially Sérgio Graça for being available and to Alexandra Jacques for the sympathy, understanding and care put in all my daily affairs in the Department of Materials Engineering at IST.

To Dr. Arlindo Almeida I owe the initial idea for the study and the sialoliths providing. I am in debt to my co-supervisor Prof. António Pedro Alves de Matos for his patience and kindness in explaining me some of the basic biologic concepts and ideas used in the text. Most importantly, credits should be given to him for the proposed mechanism for sialolith formation. Finally, I would like to thank my dear Prof. and friend Patrícia her encouragement, undying patience and generosity throughout this long and sometimes tortuous project, one that I am sure I would never see the end of without her precious help. For your knowledge, hard work and common sense, thank you! I have really learned a lot with you Prof. Patrícia!

Olga Santo

Lisbon, October 2008

Table of Contents

Abstract

Characterization of morphologic, structural and chemical aspects of a series of eight sialoliths has been carried out using scanning electron microscopy combined with energy dispersive spectroscopy, attenuated total reflection Fourier transform infrared spectroscopy and atomic force microscopy techniques, as well as nuclear magnetic resonance. Although the specimens investigated presented dimensional, morphological and structural diversity, common or typical features could be inferred. Namely, the presence of one irregular core loosely connected to subsequent concentric layers, which formed either by a laminar mechanism or by a globular mechanism and alternated thereafter in succession. The laminar layers consist of fine mineralized strata intercalated with fine organic strata. Globular layers consist of alternating bands of highly calcified globules and bands where globule calcification was still in course or was even incipient. The organic matter in the globular structures and in the organic strata contains a high level of collagen, implicating fibroblasts activity and therefore connective tissue invasion. Mineral matter in the sialoliths consists essentially of hydroxyapatite. In view of the observations a mechanism for sialolith formation has been proposed. Regarding the mechanical properties, the relatively high work of adhesion to a silicon tip by the organic matter and the ductile fracture behavior observed may justify the modest success rate of shock wave lithotripsy with salivary calculi when compared with renal calculi.

Keywords Sialoliths – SEM – SE – BSE – EDS – ATR-FTIR Spectroscopy – NMR Spectroscopy – AFM Analysis.

1 Introduction

1 Introduction

Sialadenitis is a salivary gland inflammation due to obstruction of a salivary gland or duct. Sialolithiasis, one of the major causes of sialadenitis, is the formation or presence of a salivary calculus or sialolith in the intra or extra-glandular duct system. Calculi in the salivary glands can be found in 1.2 % percent of the general population [1]. Most salivary gland calculi occur in the submandibular glands (80%-90%) and in the parotid glands (5-20%). The sublingual gland and the minor salivary glands are very rarely affected [2]. Demographically, sialolithiasis shows a slight male predominance in most studies and affects mainly patients in their third to sixth decade of life. Children are rarely affected, although sialoliths in patients aged 3 weeks to 15 years old have been reported [3].

Significant factors for the high incidence of submandibular sialolithiasis seem to be the presence of viscous secretions of high alkalinity, a long length of the excretory duct and antigravity flow of saliva [4,5].

Single salivary calculi occur in 70-80% of cases [2]. Multiple sialolithiasis is rare although a few reports are available in the literature [6]. Relatively to the calculi localization in the salivary glands and ducts, parotid calculi are found in the helium or parenchyma of the gland in 50% of the cases, while submandibular calculi are found mainly in the duct system [8]. The calculi vary in size and shape. Sialoliths are tipically round or oval shaped when formed in the gland and elongated when formed in the ducts. Parotid calculi are usually smaller and more often multiple. Parotid calculi appear with a more equitable distribution of organic and inorganic matter than submandibular stones [5]. Usually single sialolith recurrence is rare and multiple sialolith recurrence is even rarer [6]. In total, the recurrence rate of sialolithiasis has been estimated to be 8.9% [2].

Sialolithiasis typically causes pain and swelling of the involved salivary gland by obstructing the food related surge of salivary secretions. Sialoliths may cause stasis of saliva facilitating bacterial ascent into the gland and subsequent infection. Some calculi may be asymptomatic as the obstruction is only partial. Long term obstruction in the absence of infection can lead to atrophy of the gland with resultant lack of secretory function and ultimately fibrosis [5].

The diagnosis of sialolithiasis is based on the characteristic history and physical examination of the patient. Recurrent pain and swelling of the gland especially during

meals are common symptoms of sialolithiasis. However, imaging techniques are of fundamental importance for a positive diagnostic: occlusal radiographs reveal radiopaque calculi while radiolucent calculi are detected through sialography. Ultrasound and computed tomography (CT) scans are also available techniques for detection of salivary stones.

Depending on the particular situation, namely the gland affected and the calculus localization, management of sialolithiasis involves different approaches, from conservative therapy to more aggressive surgical intervention. During the last years, there has been a growing interest in minimizing invasive treatment of sialolithiasis. Sialoendoscopy offers a new method for diagnostic, treatment and postoperative management of obstructive salivary gland diseases. Endoscopy techniques reveal a success rate of 86% in parotid sialolithothomy and 89% in submandibular sialolithotomy [9]. Extracorporeal shock wave lithotripsy (ESWL) and endoscopic intracorporeal shock wave lithotripsy (EISWL) are other non-invasive therapeutic techniques available to treat sialolithiasis. These procedures use shock waves to shatter salivary calculi enabling the fragments to pass out of the duct. However, shock wave lithotripsy has only achieved modest success in salivary calculi removal (30 to 45% success rate) [19-24].

The structural diversity of sialoliths has been studied and reported by several authors [4,5,16]. There are not only differences in structure and mineralization between sialoliths but also some variability within a single sialolith [4]. In general, sialoliths consist of one or more mineralized cores surrounded by laminar layers of organic and inorganic strata. Chemically, the inorganic matter consists essentially of calcium phosphate and calcium carbonate in the form of hydroxyapatite although other crystallographic forms of calcium phosphate may be present [10]. The organic components have been reported to be essentially glycoproteins, mucopolysacharids, lipids and cell detritus [4]. The concentration of organic matter is predominant in the outer shell [4]. In this region a large zone (50-210 μm) of connective tissue and mataplastic squamous epithelium has been detected, with enzymatic activity of acid phosphatase, lactate dehydrogenase, succinate dehydrogenase and maleate dehydrogenase [4]. Uric acid calculi may form in patients with gout [5]. Some sialoliths are exclusively constituted by organic matter [11]. Energy dispersive X-ray microanalysis and X-ray photoelectron spectroscopy confirmed that major elements

present in sialoliths are Ca, P, O, C and N with small amounts of Mg, Na, Cl, Si, Fe, K and S [12-16].

The exact mechanism involved in sialolith genesis remains largely unknown but several theories have been proposed to explain the etiology and pathogenesis of salivary calculi. Theories defending an initial organic nidus or, alternatively an initial precipitation of minerals, with subsequent deposition of organic and inorganic layers, can be found in the literature [4,5,10,11,]. Nevertheless, it remains object of discussion the reasons that unchain the formation of the first nidus or initial precipitation. Infection or inflammation of the gland, bacterial proliferation, viscous nature of the mucous secretions, all have been suggested as factors for calculus etiology. The differences in etiology of calculi extend to its localization in the salivary gland or duct system. Submandibular calculi are thought to form around a nidus of mucous, whereas parotid calculi may tend to form around a nidus of inflammatory cells or a foreign body [5].

Although an exhaustive and systematic organization of the theories on etiology and development of salivary calculi has not been carried out here, it is clear that successive improvements and diversification of technical means open new perspectives into the theme investigation.

The purpose of the present work is the characterization of morphologic, structural and chemical aspects of eight sialoliths using scanning electron microscopy (SEM) combined with energy dispersive spectroscopy (EDS), attenuated total reflection Fourier transform infrared spectroscopy (ATR-FTIR) and atomic force microscopy (AFM) techniques, as well as nuclear magnetic resonance spectroscopy (NMR).

Analysis of sialoliths by NMR and AFM techniques has never been reported in the literature to the author's best knowledge.

2 Materials and Methods

2 Materials and Methods

The sialoliths were extracted in the Maxillofacial Surgery Service of S. José Hospital-Lisbon and kept dry in medical containers. Sialolith 4 was maintained in formaldehyde and left drying to air during 48 hours before observation. Available general characteristics of the sialolith donors are summarized in Table 1.

Table 1. Characteristics of sialolith donors

	Sialolith number							
Donors characteristics	1	2a)	2b)	3	4	5	6	7
Age (years)	46	66	66	69	-	-	24	39
Sex	Female	Male	Male	Female	Female	Female	Female	Female
Origin site	-	Right submaxillar	Right submaxillar	-	-	-	Right submaxillar	-
Clinical evolution (years)	1	-	-	14	-	-	11	3

The investigations types carried out on each sialolith are summarized in Table 2. Due to the reduced size of some sialoliths and to the incompatibility of preparation methods not all investigation types could be carried out with all sialoliths.

Table 2. Investigation types

	Sialolith number							
Investigation Type	1	2a) [1]	2b) [1]	3	4	5	6[2]	7
External morphology	☑	☑	☑	☑	☑	☑	☒	☒
Fracture surface	☑	☒	☒	☒	☒	☑	☒	☒
Polished cross-section	☑	☑	☑	☑	☑	☑	☒	☒
ATR-FTIR	☒	☒	☒	☑	☒	☒	☒	☒
RMN	☑	☒	☒	☒	☒	☒	☑	☑
AFM	☒	☒	☒	☑	☒	☒	☒	☒

[1] Same donor.
[2] Fragmented (crumbled) during preparation.

2.1 Scanning Electron Microscopy and Energy Dispersive X-Ray Spectroscopy

Scanning electron microscopy is a versatile technique capable of producing images with resolution around 1 nm. The scanning electron microscope includes a source of high-energy electrons (thermionically emitted from a tungsten or lanthanum hexaboride cathode or alternatively generated via field emission) which are accelerated towards an anode; and a condenser system, composed by electromagnetic lenses to focus the electron beam into a fine probe (sized 1 nm to 5 nm) that impinges on the specimen. The beam passes then through pairs of scanning coils, which deflect it horizontally and vertically so that it scans in a raster fashion a rectangular area over the sample surface.

When the primary electron beam is focused on the material, the electrons lose energy by repeated scattering and absorption within a teardrop-shaped volume of the specimen known as the interaction volume, which extends from less than 100 nm to around 5 µm into the sample. The spatial resolution is primarily defined by the size of this interaction volume which depends on the beam accelerating voltage, the average atomic number of the specimen and the specimen´s density.

Secondary electrons (SE) are electrons emitted from the specimen with energy less than 50 eV, and are generally produced as a result of interactions between energetic primary electrons and weakly bound conduction electrons in the sample. An important characteristic of SE is their shallow sampling depth, a direct consequence of the low kinetic energy with which they are formed [25], and that justifies the high spatial resolution attainable with this signal type (less than 1 nm at the state of the art). SE are detected at each point and the resulting signal is rendered into a two-dimensional intensity distribution that can be viewed and saved as a digital image. The brightness of the SE signal depends on the number of electrons reaching the detector. If the beam enters the sample perpendicularly to the surface, then the activated region is uniform about the axis of the beam and a certain number of secondary electrons "escape" from within the sample. As the angle of incidence increases, the "escape" distance of one side of the beam will decrease, and more secondary electrons will be emitted. Thus steep surfaces and edges tend to be brighter than flat surfaces, and this results in topographical images with well-defined, three-dimensional appearance.

Backscattered electrons (BSE) are high energy electrons and can escape from a much larger volume than SE. The intensity of this signal type depends on the average

atomic number of the specimen but is more modestly dependent on topography. BSE images have lower spatial resolution than SE images due to their larger volume of origin, but can show contrast between areas with different chemical composition, since the signal intensity increases with the average atomic number in the sample.

In the present work, scanning electron microscopy observations, under secondary electron and backscattered electron modes, as well as energy dispersive spectroscopy point analyses and mapping, were carried out with a Hitachi S2400 microscope operated at 25 kV and equipped with a standard Rontec EDS detector. The observed samples were mounted in metallic supports and coated with carbon in a Polaron E-5100 coating unit prior to observation to prevent charging. Some details of the polished cross-sections were subsequently observed with a JEOL 7001F field emission SEM operated at 15 kK and equipped with an Oxford EDS detector.

The scanning electron microscopy work consisted in:

1. Acquisition of topographic images to obtain the complete morphologic description of the exterior surface of the sialoliths. Some details were recorded under SE mode, other under BSE mode. EDS point analysis and X-ray mapping were also carried out.
2. Observation of fractured cross-sections to obtain structural and chemical information. This type of observation was only carried out for larger sialoliths. The specimens were roughly cut/fractured with a scalpel through the longitudinal plan of symmetry (except for sialolith 5 which was fractured along its mid transversal section). The fractured surfaces were registered under SE and BSE modes combined with EDS point analysis and X-ray mapping.
3. Observation of polished cross-sections to obtain structural and chemical information. This type of observation was carried out on fractured halves of larger sialoliths and on smaller sialoliths. The specimens were embedded in an epoxy resin by cold mounting. After a polymerization period of 24 h, the non embedded part of the samples was cut and kept for subsequent spectroscopic analysis (Figure 1). Special care was put into this operation to avoid contamination of the samples. The resin embedded cross-sections were grounded with SiC paper and polished using alumina suspensions in water. Images were acquired essentially under BSE mode combined with EDS point analysis and X-ray mapping.

The types of observation performed on each sialolith are listed in Table 2.

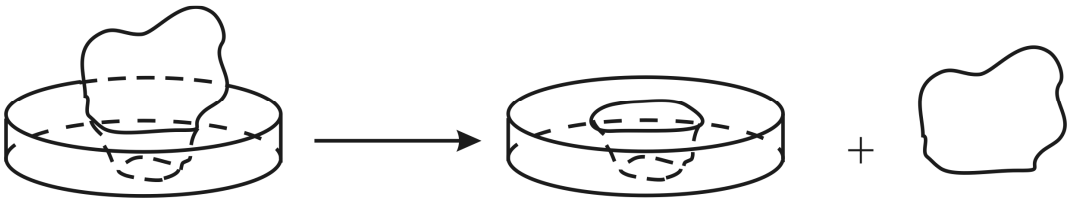

Figure 1. Embedding procedure yielding a mounted sample, which was subsequently polished and used for ultrastructural observation and ATR-FTIR spectroscopy, and a non-embedded part used for RMN spectroscopy.

2.2 Attenuated Total Reflection- Fourier Transform Infrared Spectroscopy

Infrared radiation (IR) is absorbed by organic molecules and converted into energy of molecular vibration, either stretching or bending. Different types of bonds, and thus different functional groups, absorb infrared radiation of different wavelengths. IR spectra are interpreted by extrapolating from simple molecule studies, since most functional groups give rise to bands in particular regions of the spectrum. The region from 4000-1300 cm^{-1} is particularly useful for identifying the presence of specific functional groups.

The key components of a Fourier Transform (FT) system are the source, the interferometer and the detector. Since no detector can simultaneously sense the intensity and frequency of IR radiation with practical results, one of these two variables must be kept constant. The problem is solved using an interferometer to modulate the IR source intensity by changing the position of a reflecting mirror which reflects light from the source towards the sample. Thus, the interferometer provides a means for the spectrometer to measure all optical frequencies simultaneously by modulating the intensity of individual frequencies before the detector picks up the signal. The product of an interferometer scan, termed interferogram (a plot of intensity versus mirror position), cannot be interpreted in its original form. A Fourier transform is the required to convert the interferogram into a spectrum, i.e. intensity versus frequency or wavenumber.

The interaction between an IR beam and a target sample can occur in many ways, which makes FTIR a versatile tool. The following modes of IR analysis have

been developed over the years: IR transmission, IR reflectance, IR specular reflectance, IR diffuse reflectance and ATR-FTIR.

ATR-FTIR spectra are obtained by pressing the sample against an "internal reflection element", IRE, (e.g. ZnSe). IR radiation is focused onto the end of an IRE and reflects across the length of the crystal. IR radiation actually penetrates one micron from the surface of the IRE into the material. Key advantages of this configuration are its high spatial resolution and the possibility to investigate opaque solid materials.

ATR Spectra were acquired from the polished cross-section of sialolith 3 using a Nicolet Nexus ATR-FTIR spectrometer coupled with a Continuμm microscope equipped with a silicon crystal, at a spatial resolution around 3 mm and at a spectral resolution of 8 cm^{-1} in the 400 to 4000 cm^{-1} range. Spectra were collected both at weakly and highly mineralized regions, as well as at the embedding resin. The background spectrum was obtained using the same settings but without contact with the sample surface. The OMNIC software package was used for the spectra treatment, which involved co-adding 200 scans for background, sample measurements and embedding substrate.

2.3 Nuclear Magnetic Resonance Spectroscopy

NMR is a phenomenon which occurs when unpaired spin nuclei are immersed in a static magnetic field and exposed to a second oscillating magnetic field. In solution NMR spectra consist of a series of very sharp transitions, due to averaging of anisotropic NMR interactions by rapid random tumbling. By contrast, solid-state NMR spectra are very broad, as the full effects of anisotropic or orientation-dependent interactions are observed in the spectrum. High-resolution solid state NMR spectra can provide the same type of information that is available from corresponding solution NMR spectra, but a number of special techniques are needed, such as magic-angle spinning and cross polarization.

Anisotropic dipolar interactions can be suppressed by introducing artificial motions on the solid. This technique involves rotating the sample about an axis oriented at 54.74° with respect to the external magnetic field. This became known as magic-angle spinning (MAS). Samples are finely powdered and packed tightly into rotors, which are then spun at rates from 1 to 35 kHz, depending on the rotor size and type of experiment being conducted.

When combined with MAS, polarization from abundant nuclei like ^{1}H, ^{19}F and ^{31}P can be transferred to dilute or rare nuclei like ^{13}C, ^{15}N, ^{29}Si in order to enhance signal to noise and reduce waiting time between successive experiments.

A Bruker MSL 300 P spectrometer was used to observe ^{13}C resonance at 75.47 MHz. ^{13}C (with ^{1}H cross-polarization and decoupling). MAS spectra were acquired from powdered sialoliths 6 and 7 (Table 2) at spinning rates of 4 kHz at around 22 ºC. A 7 mm o.d. zirconia rotor was used in the experiments. The external references for ^{13}C chemical shifts were glycine (CH_2, 41.4 ppm). The accuracy of the ^{13}C peak positions was 0.159 ppm.

The non-embedded parts of sialolith 1 were powdered and used to produce a preliminary NMR spectrum, which presented low signal/noise ratio due to the reduced sample volume. Sialolith 6, which was coated with carbon for SEM observation but fragmented during preparation, was entirely reduced to powder for NMR investigation. However, the carbon coating induced adverse effects on the NMR spectrum and another specimen, sialolith 7, that was not observed by SEM and was not coated with carbon, was completely reduced to powder and used for NMR investigation as a control specimen.

2.4 Atomic Force Microscopy

Scanning in constant force mode perpendicularly to the longitudinal axis of the cantilever, gives rise to cantilever twisting as a result of surface relief and friction forces, in addition to deflection in the normal direction. The simultaneous measurement of deflection and twisting with a sensitive four-sectional detector permits the simultaneous acquisition of topographic and frictional information over the sample surface. To separate the tribological effect from the topographic effect, two topographic images are recorded, one during the trace of each scan and the other during the retrace. Under ideal conditions, the subtraction of these two image types eliminates topographic information and amplifies frictional information, rendering frictional force distributions. A lateral force microscopy (LFM) image is hence obtained offering direct visual information about differences in chemical composition of a surface.

Force spectroscopy (FS) is used to measure forces of interaction between the probe tip and the surface sample as a function of their distance. The base of the cantilever is moved slowly in the vertical-z direction towards the sample surface and

retracted again after contact or indentation (or vice versa). This technique provides information on local elastic properties and work of adhesion.

Topographic images were obtained under contact mode in specific areas of sialolith 3 polished cross-section. Both the trace and retrace images were recorded and LFM was carried out by subtracting the retrace image from the trace image. FS was used to obtain force-distance curves at selected points of the sample enabling to assess work of adhesion variations. AFM/LFM/FS work was performed at room humidity and temperature with a Veeco DI CP-II atomic force microscope using commercially available silicon cantilevers (MPP 31100-10, Veeco), with nominal length of 450 μm and nominal spring constant of 0.9 N/m.

3 Results

3 Results

3.1 Scanning electron microscopy

The results in this section comprehend images obtained from external surfaces, fractured surfaces and polished cross-sections, and are grouped by sialolith. EDS point analysis and X-ray maps consistently showed that bright regions under BSE imaging mode were Ca and P-rich, whereas darker contrast regions consisted of organic matter containing S. The former are therefore highly mineralized regions while the latter are weakly mineralized regions.

Sialolith 1

External morphology

Sialolith 1 presented an approximately spherical shape with a diameter of about 8 mm (Figure 2). The relatively fine external topography evidenced calcium phosphate microcrystals (Figure 3) with a morphology compatible with monoclinic brushite [10,11]. Local bulges with diameters around 500 μm were frequent at the calculus surface (Figure 4).

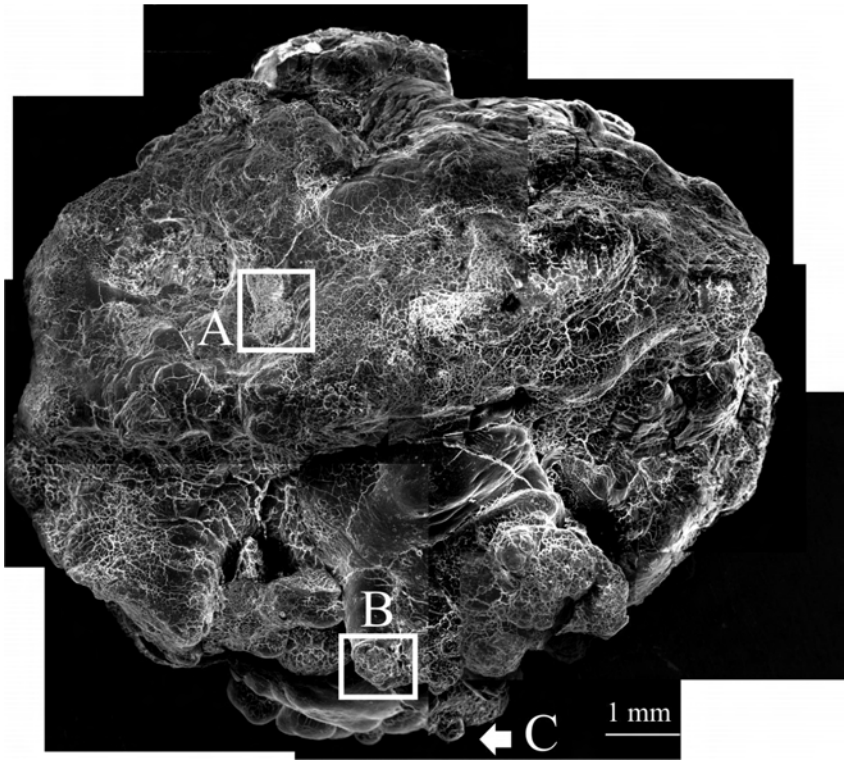

Figure 2. External surface of sialolith 1 (SE mode).

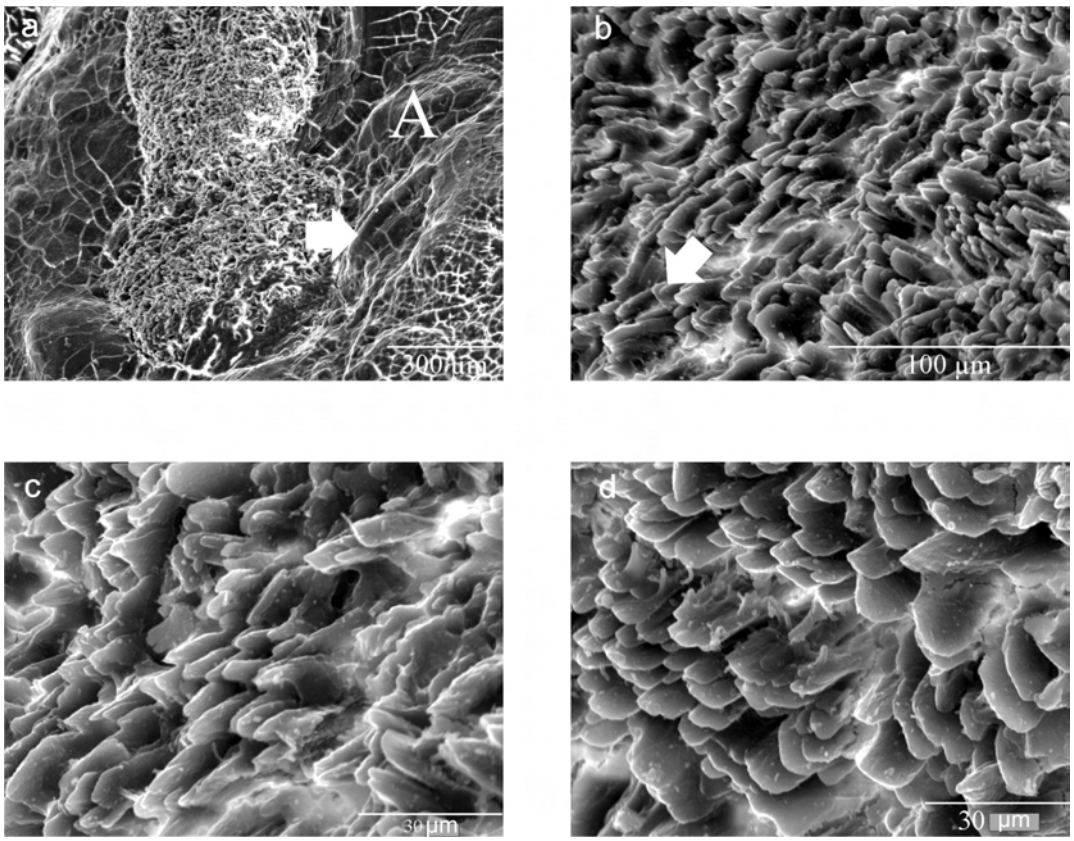

Figure 3. (a) rhough (c) Detail A of sialolith 1 external surface (SE mode) showing calcium phosphate crystals. (d) Another similar region.

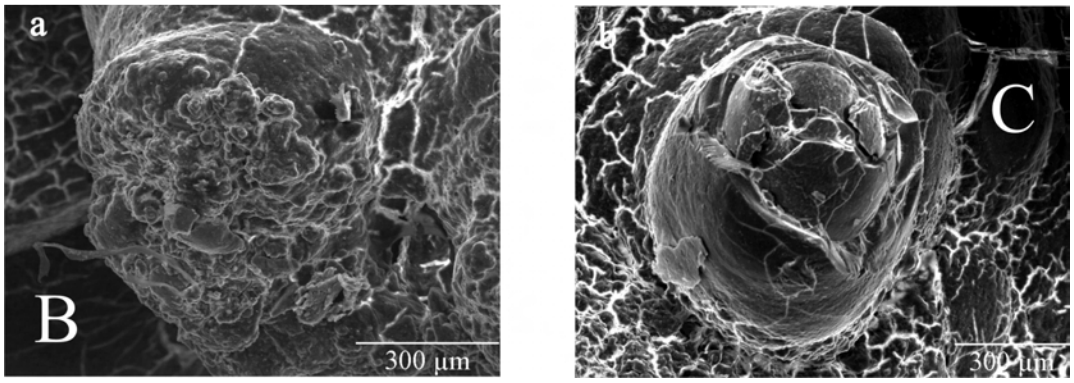

Figure 4. Details B and C of sialolith 1 external surface (SE mode).

Fracture surface

The fracture surface of sialolith 1 is shown in Figure 5. Magnified details are presented in Figure 6. Detail A discloses a large region of organic matter with low BSE contrast. Detail B presents a 250 μm thickness stratum consisting of similar organic matter. Figure 7 exhibits EDS spectra obtained at dark and bright contrast regions. The bright regions are strongly mineralized with peak proportions pointing to hydroxyapatite. The dark regions are organic matter yielding a weak X-ray signal (notice the background level) comprehending an intense S peak and minor Cl and K peaks, as well as Ca and P peaks which indicate a partial mineralization process.

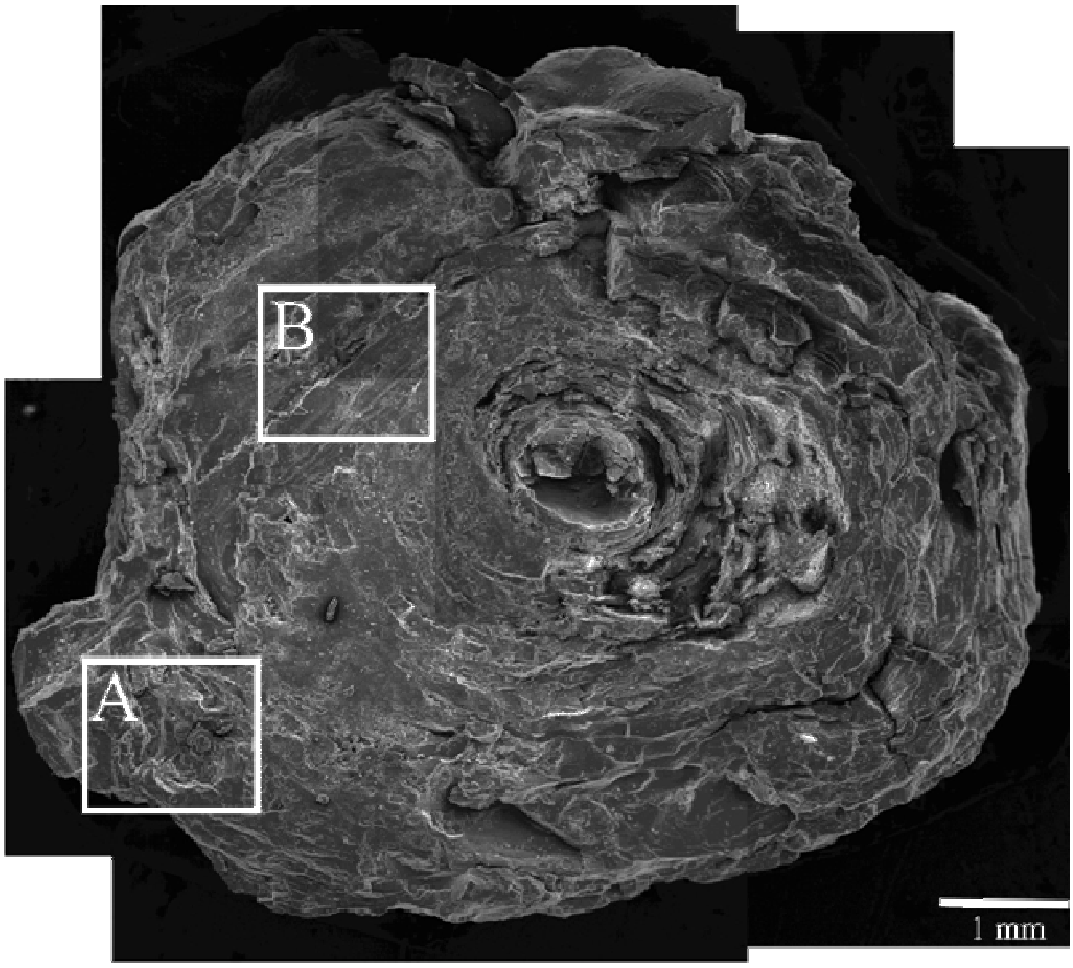

Figure 5. Fracture surface of sialolith 1 (SE mode).

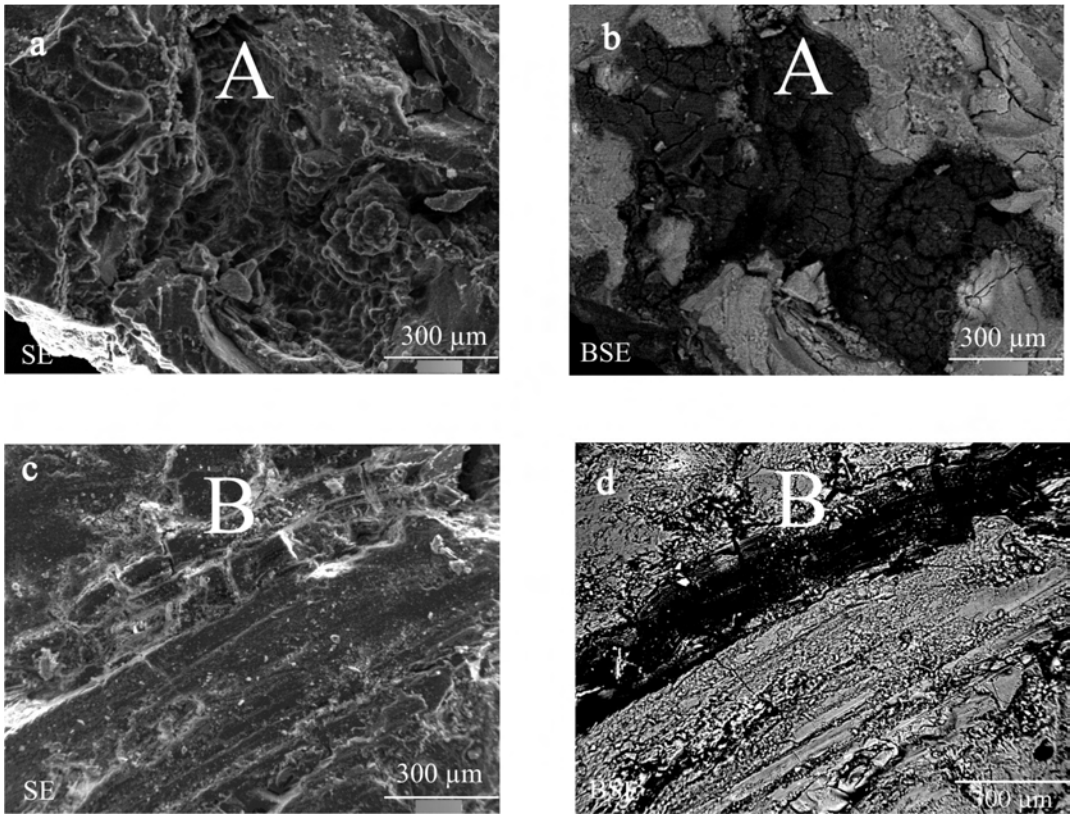

Figure 6. Details A and B of sialolith 1 fracture surface. The images on the left were obtained under SE mode, whereas the images on the right were obtained under BSE mode at the same regions.

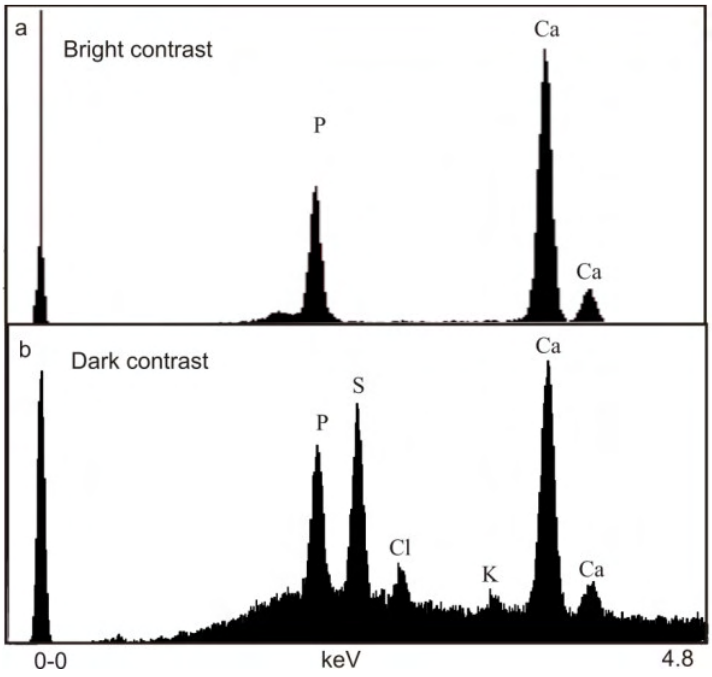

Figure 7. Typical EDS spectra obtained at (a) bright and (b) dark regions.

Polished cross-section

Figure 8 displays the polished cross-section of sialolith 1. The calculus presents one central, irregular, and highly mineralized core surrounded by a collar of teardrop globules of organic matter partially mineralized (Figures 9 and 10). An incomplete layer of these globular structures was again found at a more external region. The remaining area of the calculus consisted of convoluted and highly mineralized thick layers with patches of globular regions.

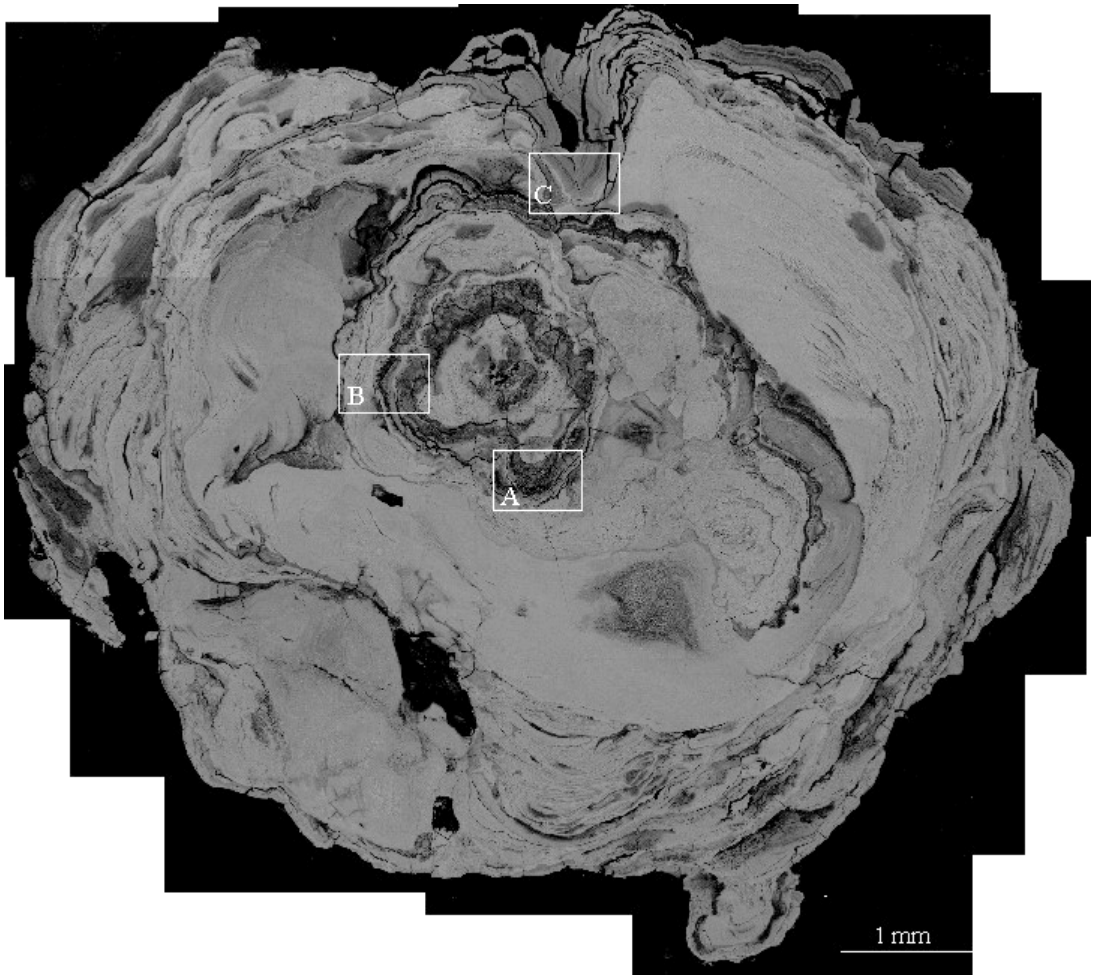

Figure 8. Sialolith 1 polished cross-section (BSE mode).

Close examination of the globular structures revealed different levels of calcification (Figure 9 and 10). Calcification of the globules proceeded by agglomeration of Ca and P-rich flake structures at mineralization centers, and induced the formation of teardrop globule crescents around larger globules (Figure 9 (c), (d) and (e)). In some instances, distinct mineralization centers were detected in the same globule (Figure 9 (c)).

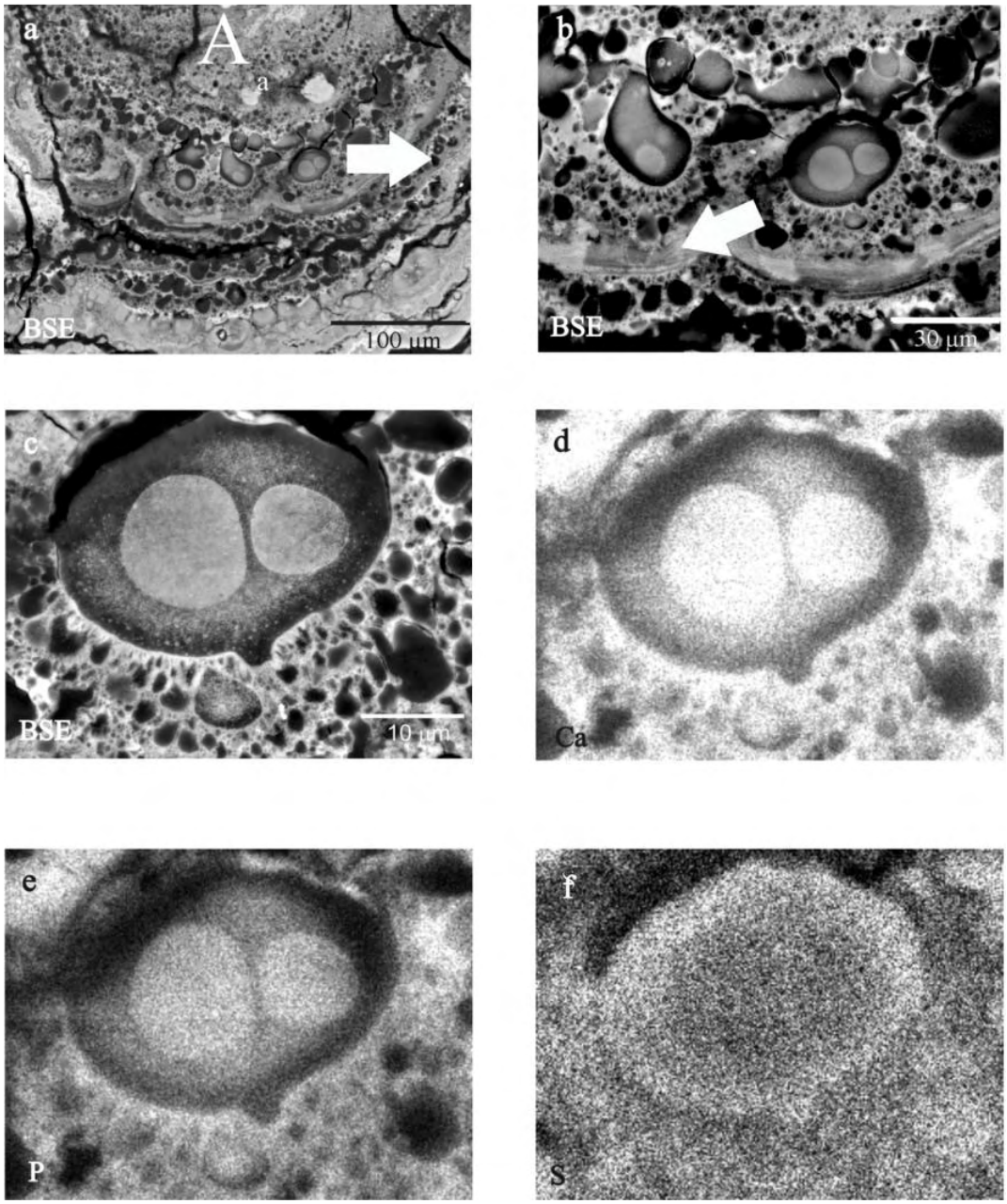

Figure 9. (a), (b) and (c) Detail A of sialolith 1 polished cross-section with successive magnifications (BSE mode). (d), (e) and (f) are respectively the Ca, P and S X-ray maps of (c).

In general, the teardrop globular layers or collars consisted of alternating bands of highly calcified globules and bands where globule calcification was still in course or was even incipient (Figure 10). Sialolith 1 lacked a clear concentric laminar layer around the core. However, some laminar layers were formed at the calculus periphery (Figure 11). The large organic matter regions detected in the fracture surface (Figure 6) were not observed in the polished cross-section due to structural variability within the sialolith.

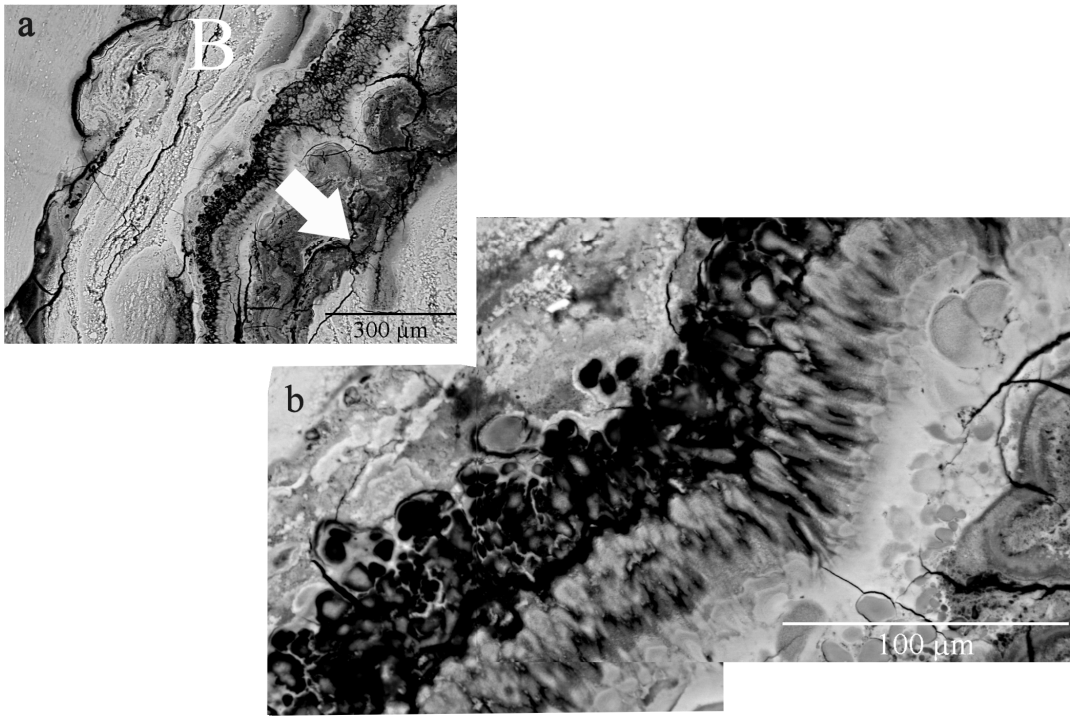

Figure 10. (a) and (b) Detail B of sialolith 1 polished cross-section with increasing magnification (BSE mode).

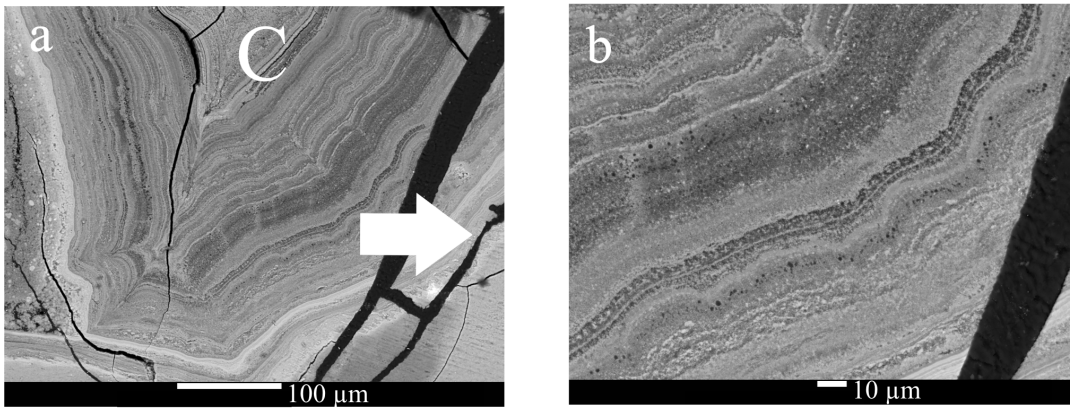

Figure 11. (a) and (b) Detail C of sialolith 1 polished cross-section with increasing magnification (BSE mode).

Sialolith 2a)

External morphology

Sialolith 2a) presented an irregular shape with approximately 9 mm of length and a diameter of 6.5 mm in its wider section (Figures 12 and 13). Bulges of ~300 μm were commonly present throughout the calculus surface. Extensive spalling and scaling were detected, but observation under BSE mode did not reveal significant chemical contrast between the exposed layers.

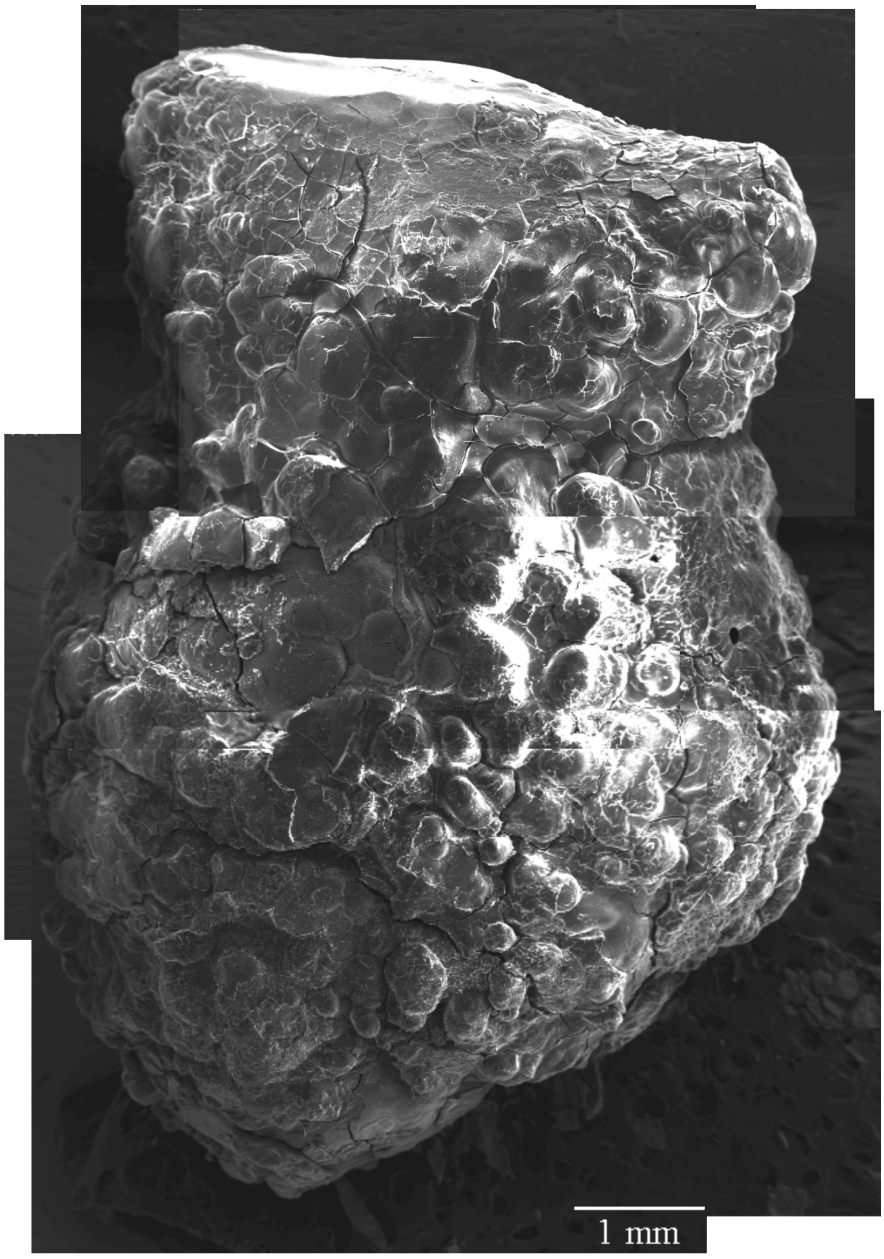

Figure 12. External surface of sialolith 2a) (SE mode).

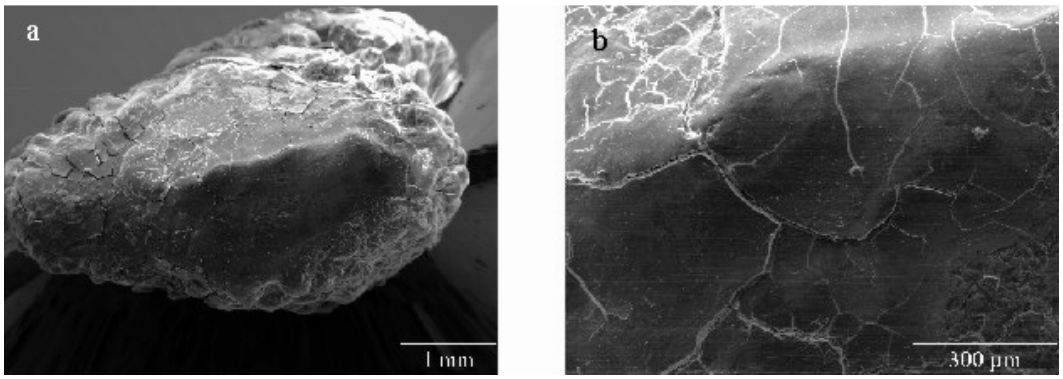

Figure 13. (a) Frontal perspective of sialolith 2a). (b) Magnified detail.

Polished cross-section

Figure 14 displays the polished cross-section of sialolith 2a). The calculus presented one irregular central core (where detail A stands), surrounded by relatively uniform and highly calcified layers with an approximately spherical surface (where detail B stands). These layers were loosely connected to the subsequent layers which underwent an extremely irregular and convoluted growth. The top "tail" suggests that at late growth stages the stone was forced to conform to the duct luminal shape. The grayscale of this low magnification image obtained under BSE mode indicates a broad range of mineralization levels in the sialolith layers. The magnified details in Figures 15 to 18 show features of the mineralization process: extensive presence of organic globules partially mineralized, teardrop collars and laminar layers. Larger globules are frequently surrounded by crescents of smaller globules with teardrop shape (see for example Figure 16 (b)).

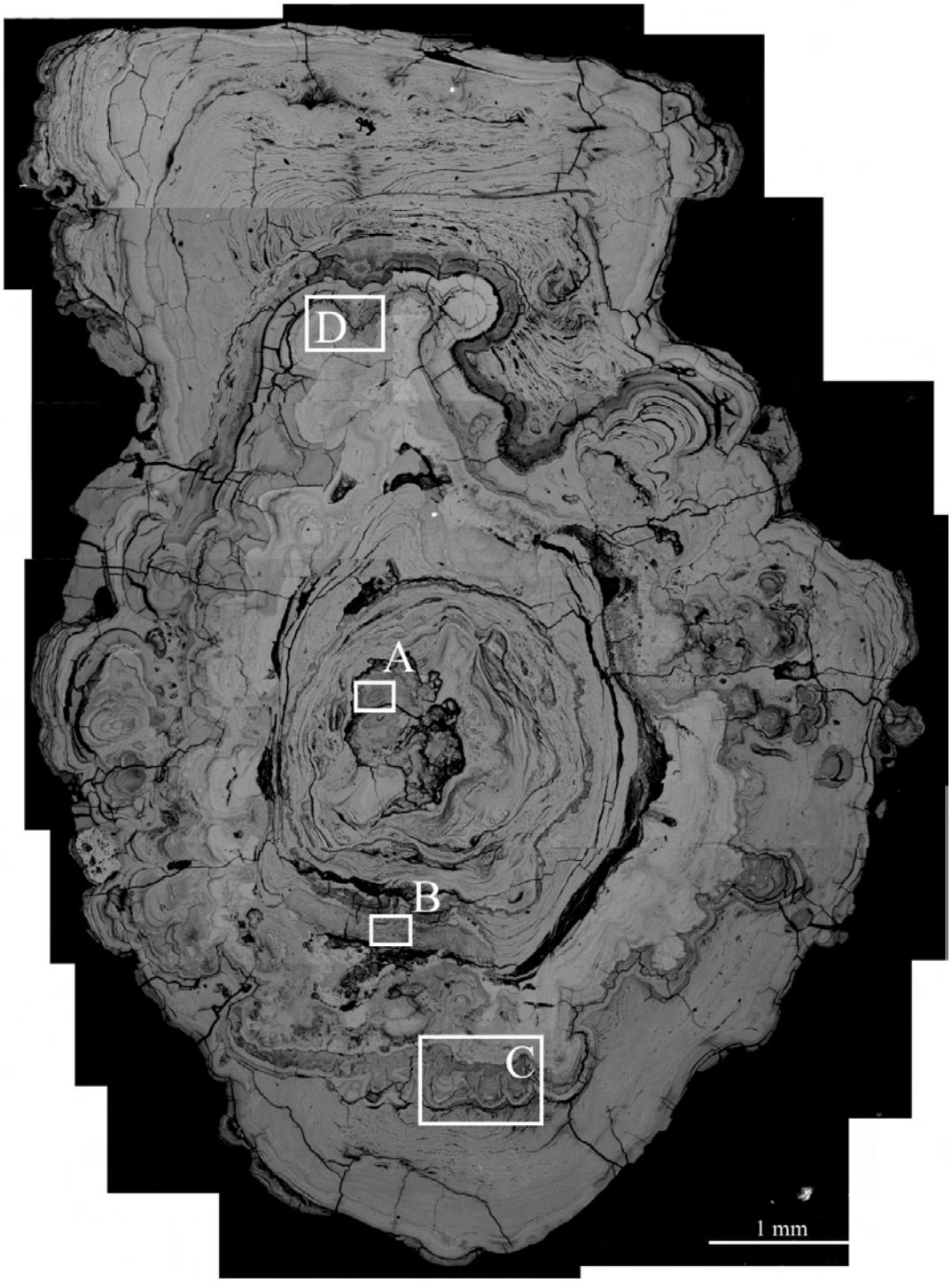

Figure 14. Sialolith 2a) polished cross-section (BSE mode).

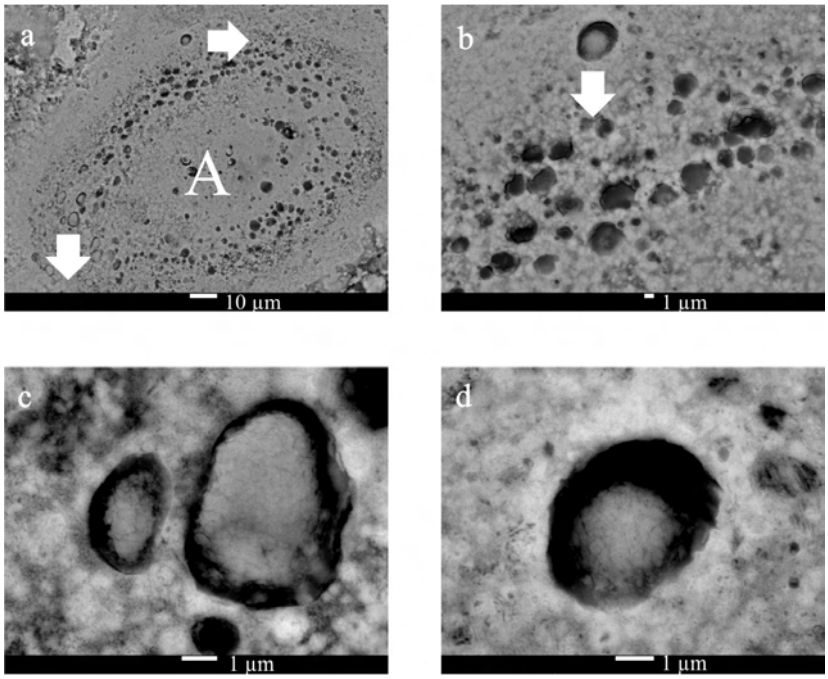

Figure 15. Detail A of sialolith 2a) polished cross-section showing mineralized layer convolutions, teardrop collars and mineralized globules.

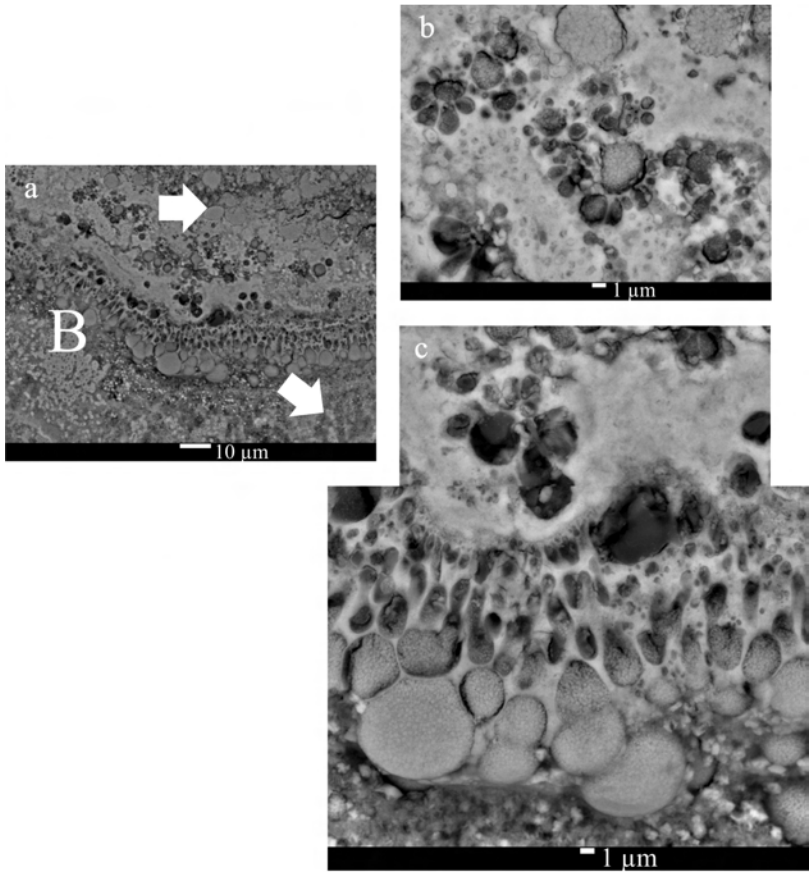

Figure 16. Detail B of sialolith 2a) polished cross-section presenting teardrop collars and teardrop crescents around globules of organic matter partially mineralized (BSE mode).

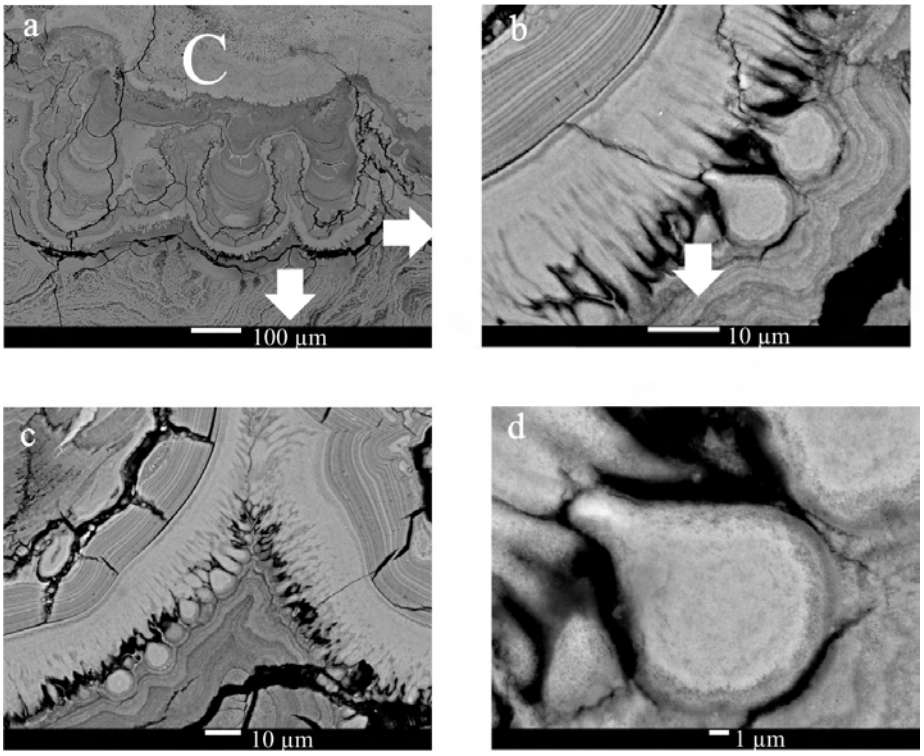

Figure 17. Detail C of sialolith 2a) polished cross-section showing an elliptically shaped region at the core severely mineralized and enclosing organic globules partially mineralized (BSE mode).

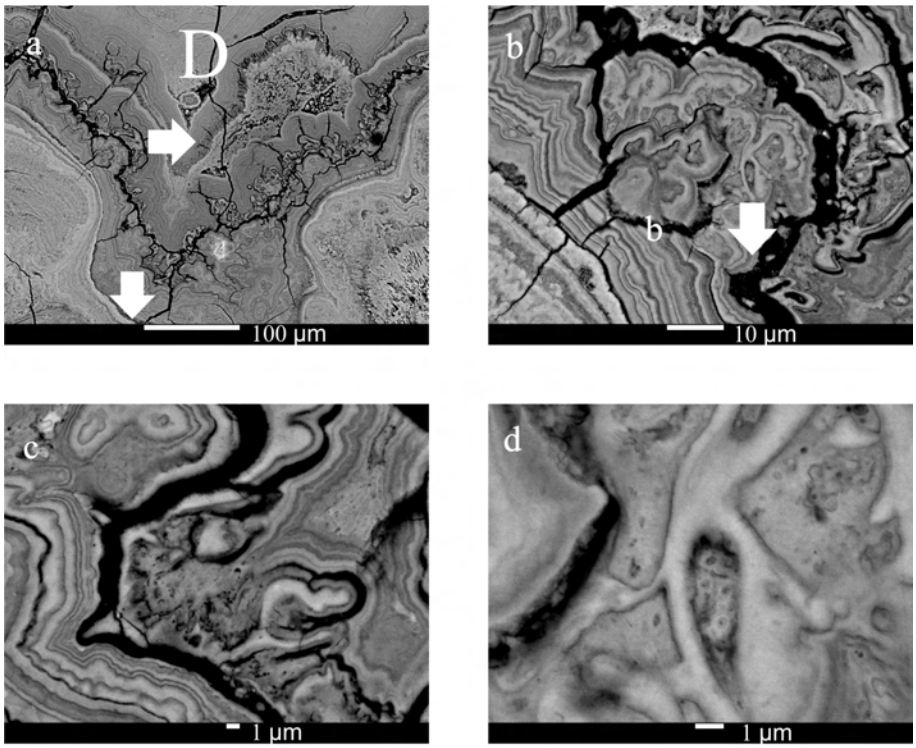

Figure 18. Detail C of sialolith 2a) polished cross-section displaying convoluted laminar layers (BSE mode).

Sialolith 2b)

External morphology

Sialolith 2b) presented an irregular oval shape with approximately 7.5 mm of length and a diameter of about 5 mm at its larger section (Figure 19). The calculus displayed generally a rough surface with extensive spalling and scaling. Careful observation under BSE mode, and EDS analyses, revealed an external layer of organic matter with ~20 μm thickness, and an underneath layer (now exposed) richer in Ca and P and exhibiting well defined mineralization crystallites (Figure 20). Bulges were frequently observed at the external surface (Figures 19 and 21). The sialolith apex was coated with a low roughness capsule, extensively microcracked and presenting circular depressions associated with organic matter (Figures 19, 22 and 23).

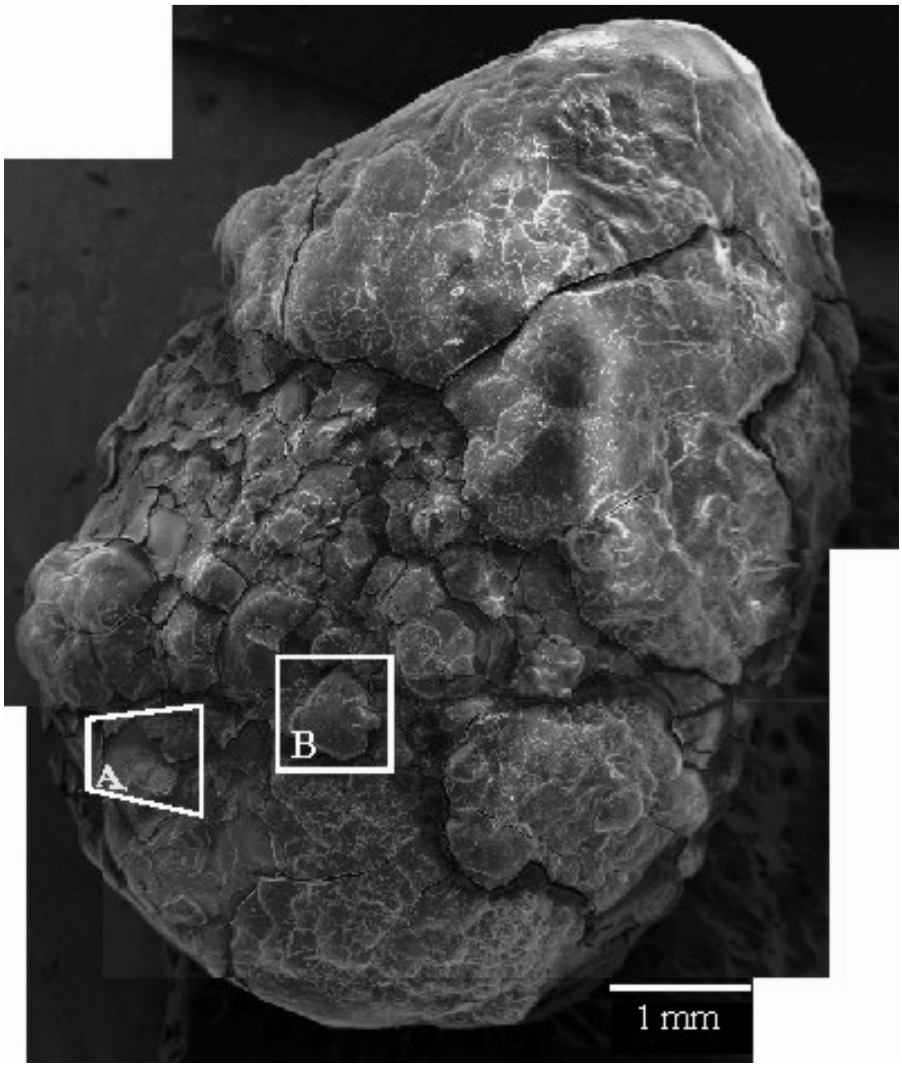

Figure 19. External surface of sialolith 2b) (SE mode).

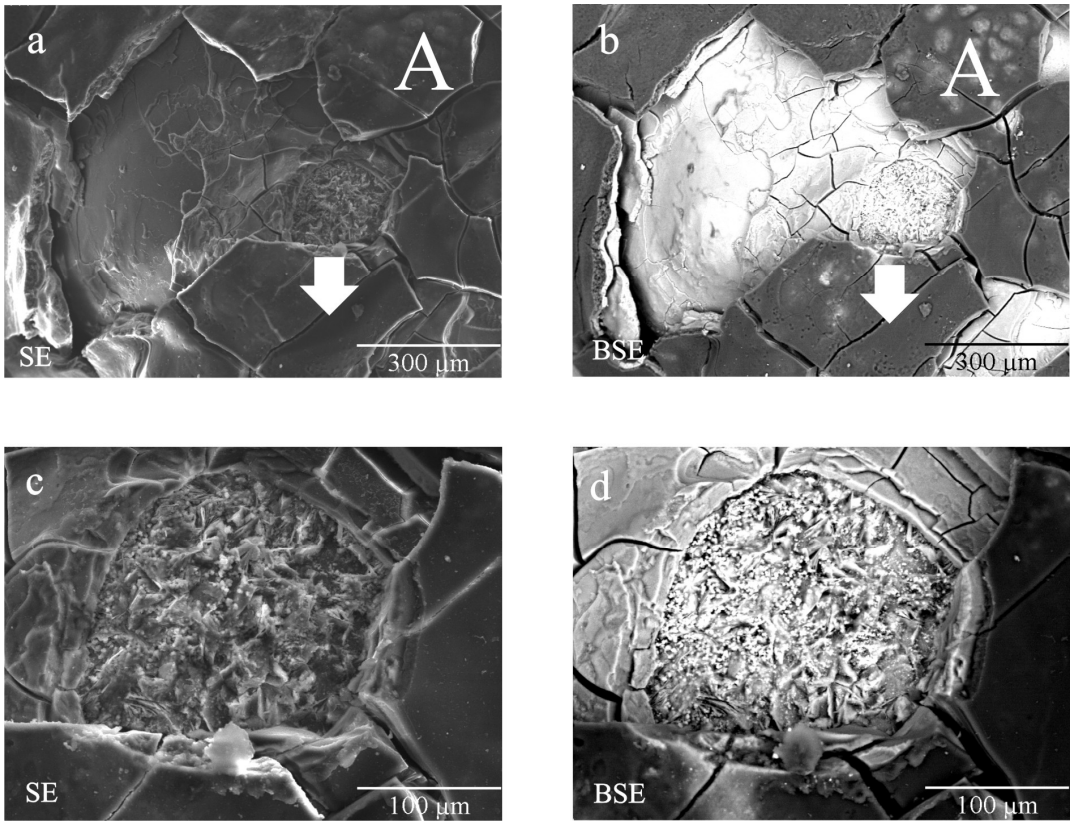

Figure 20. Detail A of sialolith 2b) external surface. The images on the left were obtained under SE mode, whereas the image on the right was obtained under BSE mode at the same region.

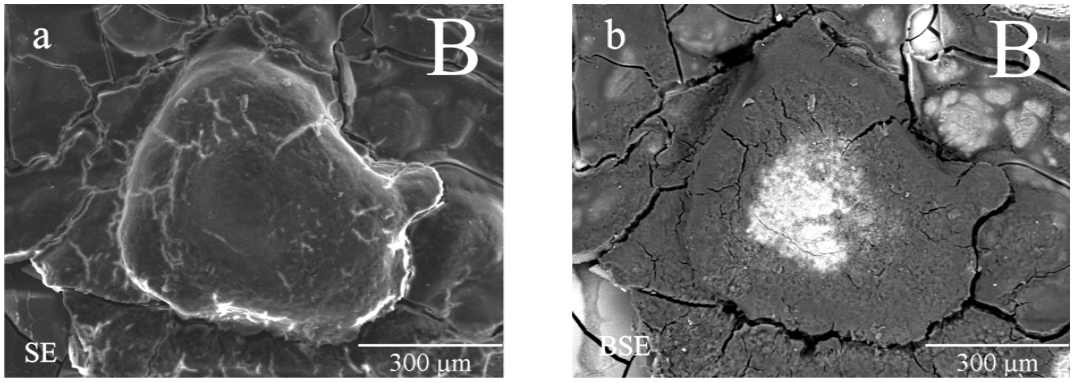

Figure 21. Detail B of sialolith 2b) external surface. The image on the left was obtained under SE mode, whereas the images on the right were obtained under BSE mode at the same regions.

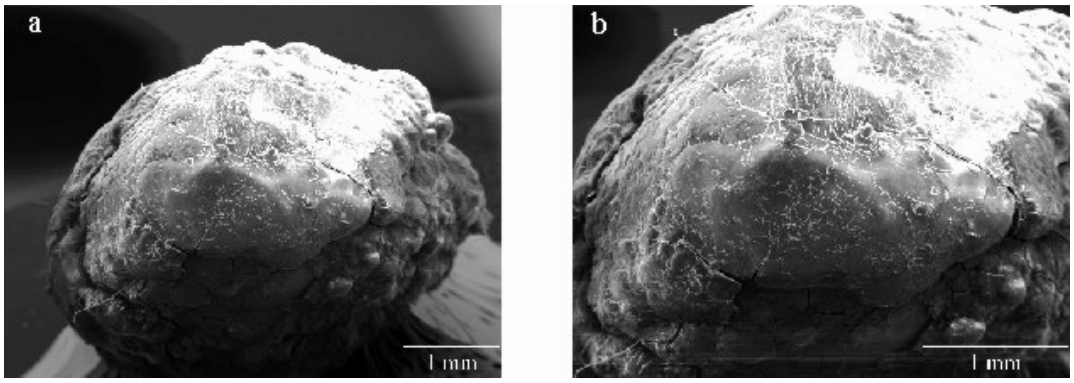

Figure 22. Frontal appearance of sialolith 2b) at different magnifications (SE mode).

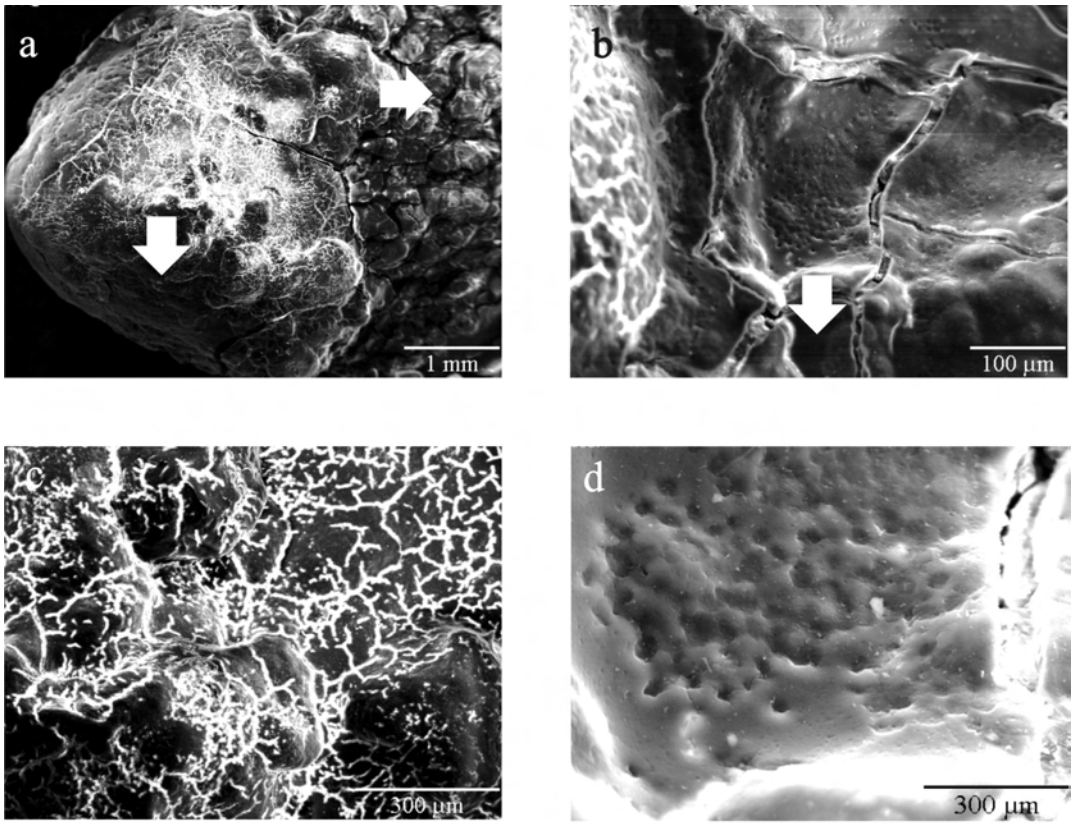

Figure 23. Frontal surface details of sialolith 2b) (SE mode).

Polished cross-section

Figure 24 displays the polished cross-section of sialolith 2b). The calculus presents one irregular and highly mineralized core located in opposition to the apex. This core is surrounded by globular structures and is loosely connected to subsequent highly calcified and regular laminar layers. The growth morphology suggests conformation to the duct luminal shape. The layer sequence clearly evidences the ultimate formation of the smooth capsule layer.

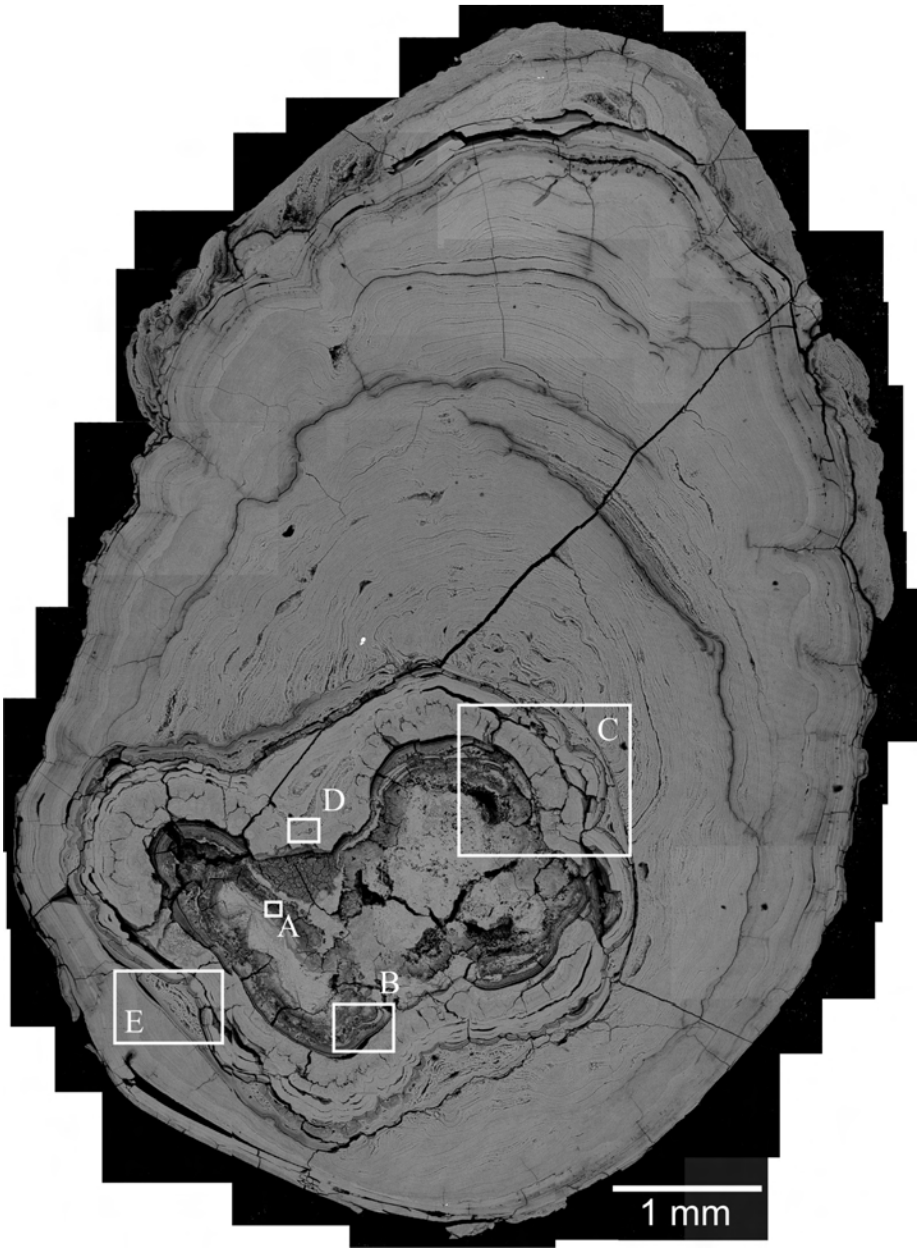

Figure 24. Sialolith 2b) polished cross-section (BSE mode).

The presence of large globules surrounded by smaller globule crescents was detected essentially at the core (Figure 25), which was surrounded by teardrop collar layers (Figure 26). The mineralization process of the globular structures proceeded via Ca and P-rich flake formation (Figures 26 (e) and (f) and 27 (d)). The layers external to the core presented a fine laminar appearance with intercalated highly and weakly mineralized strata, with an occasional presence of small mineralized spheres embedded in a less mineralized matrix (Figures 28 and 29).

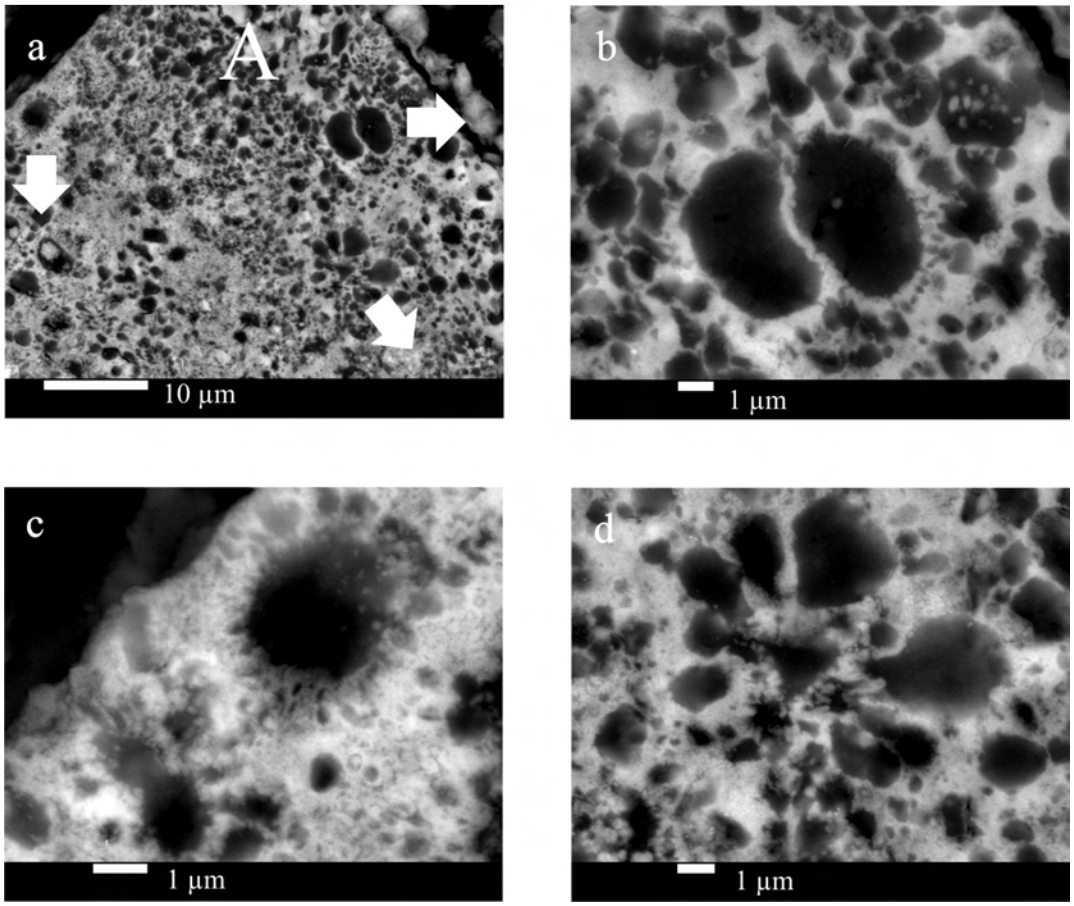

Figure 25. Detail A of sialolith 2b) polished cross-section displaying weakly mineralized globules surround by smaller globule crescents (BSE mode).

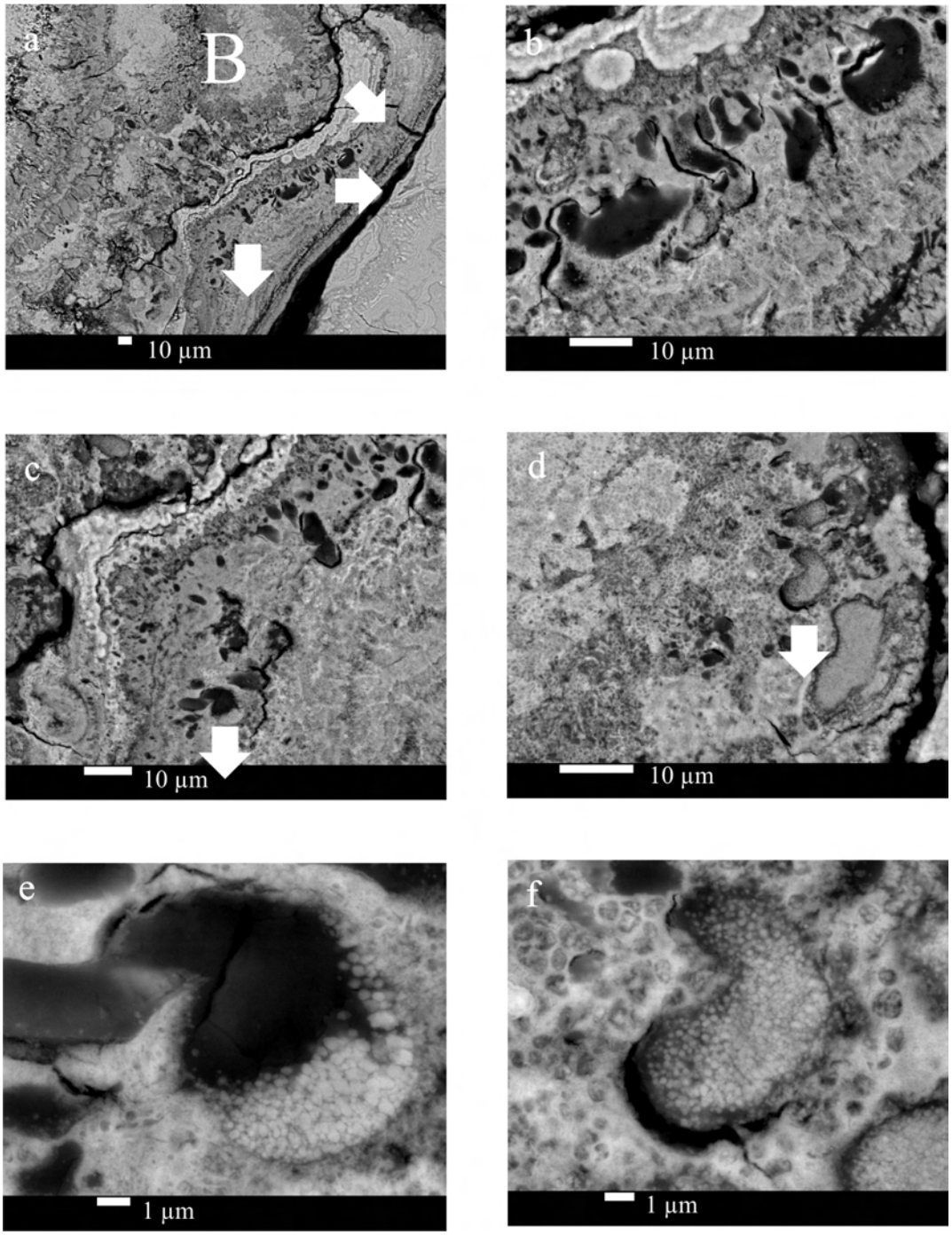

Figure 26. Detail B of sialolith 2b) polished cross-section displaying teardrop collars formed by partially mineralized globules where Ca and p-rich flakes can be resolved (BSE mode).

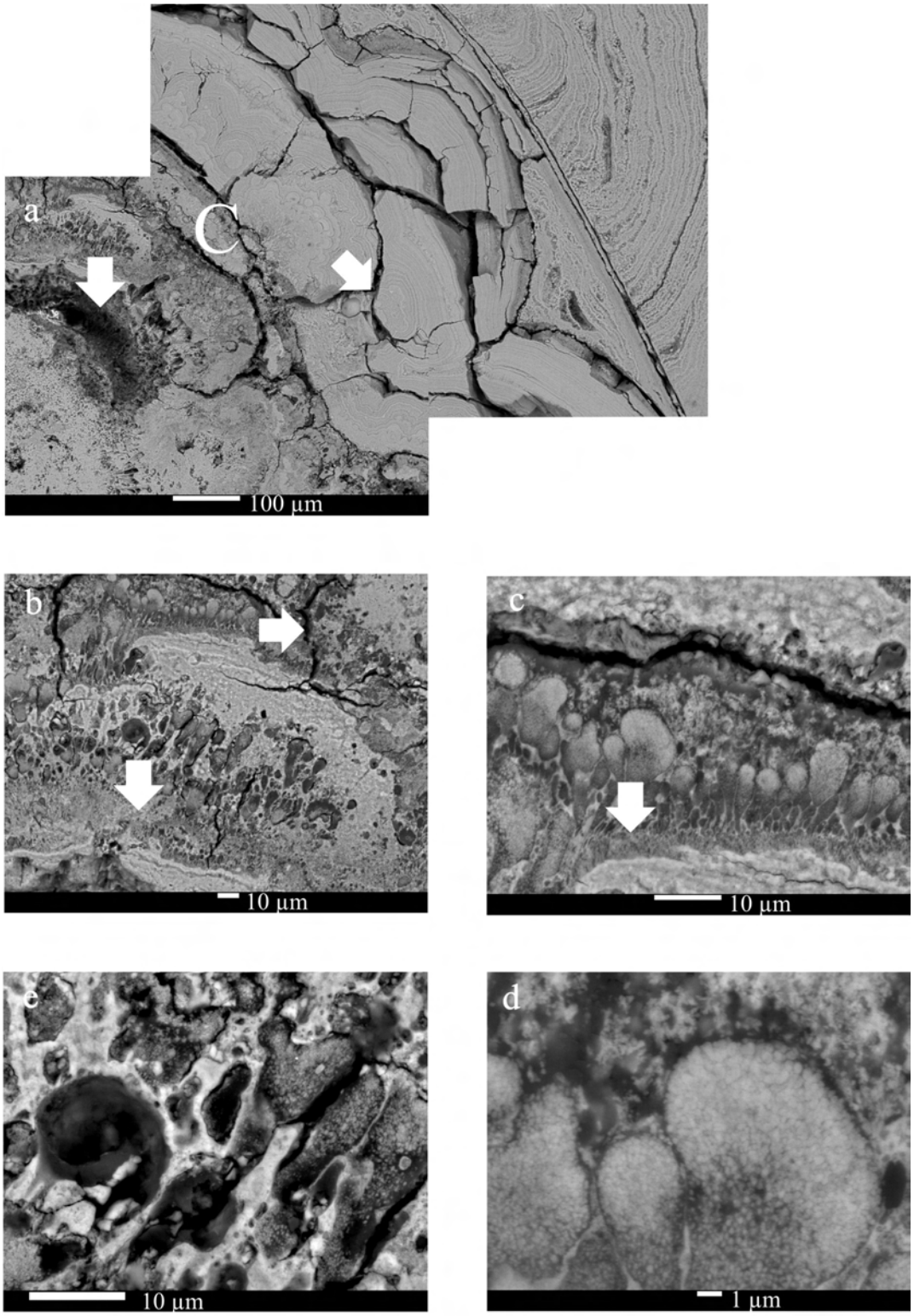

Figure 27. Detail C of sialolith 2b) polished cross-section presenting teardrop collars formed by partially mineralized globules surrounded by a highly mineralized and homogenous layer (BSE mode).

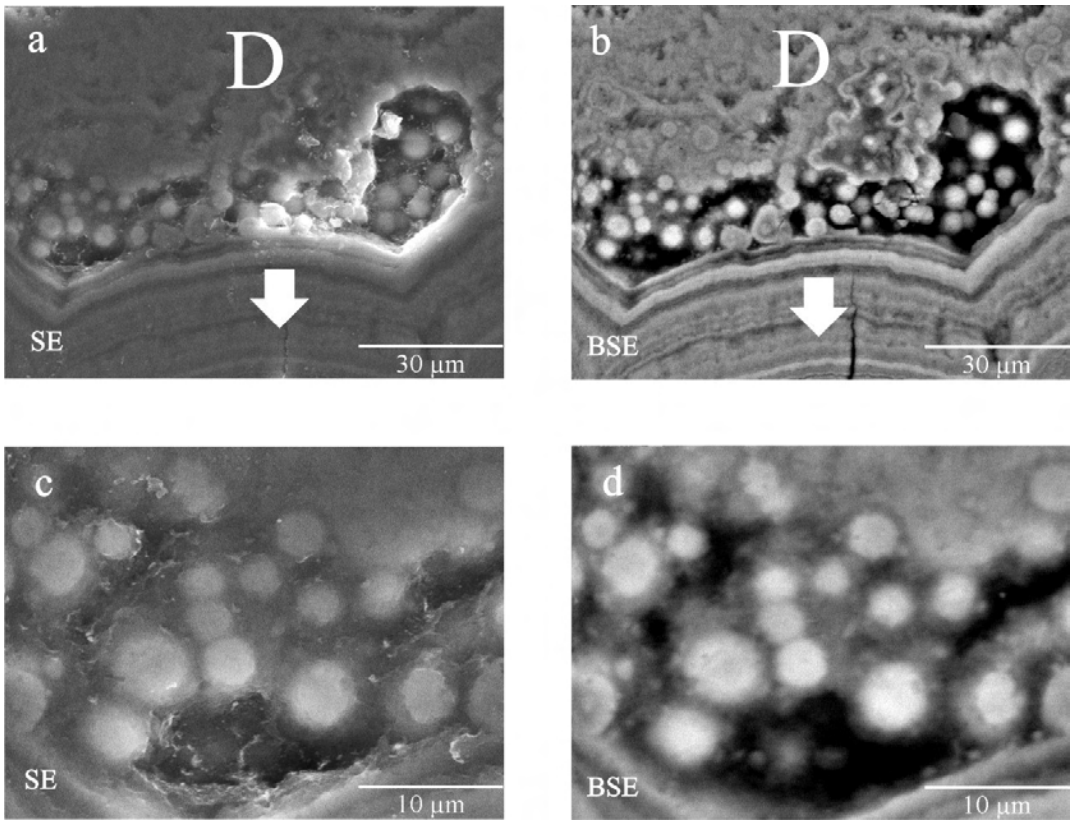

Figure 28. Detail D of sialolith 2b) polished cross-section showing a laminar layer and mineralized spheres with ~5 µm enclosed in organic matter. The images on the left were obtained under SE mode, whereas the images on the right were obtained under BSE mode at the same regions.

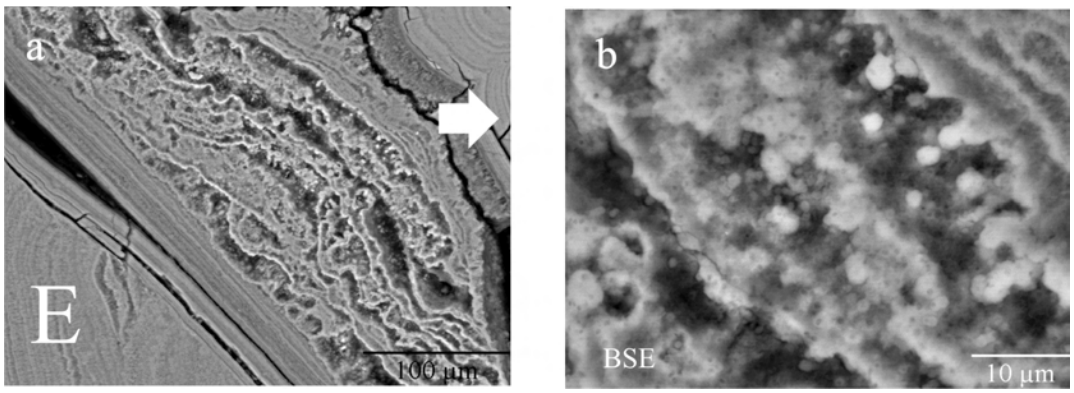

Figure 29. Detail E of sialolith 2b) polished cross-section showing a laminar layer and mineralized spheres with ~5 µm enclosed in organic matter (BSE mode).

Sialolith 3

External morphology

Sialolith 3 showed an approximately spherical shape with a diameter of about 7.5 mm (Figure 30). The calculus presented hemispheres with distinct topography: a more regular side evidencing fine bulges and invaginations (a) and a side with major cleaved and overhanging layers (b).

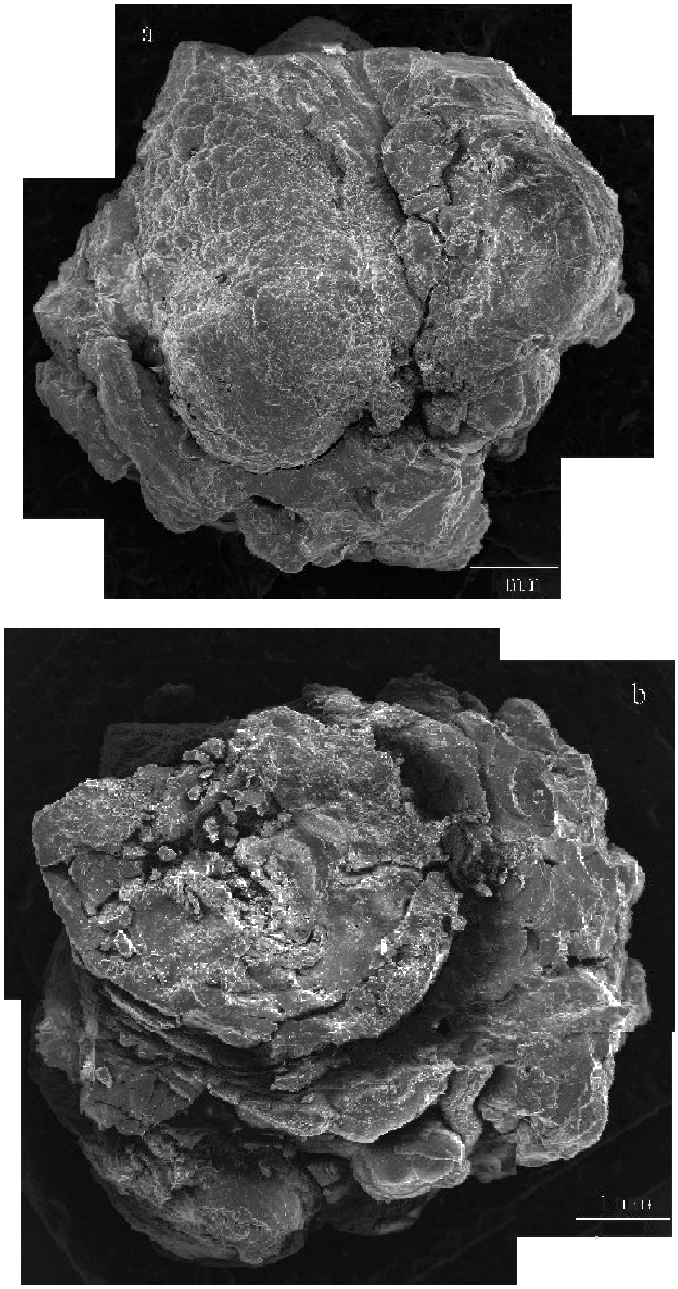

Figure 30. External surface of sialolith 3: (a) regular side (a) and (b) rough side.

Polished cross-section

Figure 31 displays the polished cross-section of sialolith 3. The calculus presents one core which is loosely connected to the peripheral layers on the left. Both the core and the peripheral regions on the right present globular structures. The two distinct surface topographies are recognizable in the polished cross-section image: the hemisphere with lower roughness (Figure 30 (a)) corresponds to the highly calcified region on the left, while the irregular surface hemisphere (Figure 30 (b)) is associated with the peripheral globular region on the right. A high concentration of globules surrounded by crescent structures could be found at the core (Figure 31). Towards the regular peripheral region, sequences of teardrop collars tended to reorganize into laminar layers (Figure 32). The globules evidenced variable degrees of calcification both at the core and at the peripheral region on the right (Figures 32 to 34).

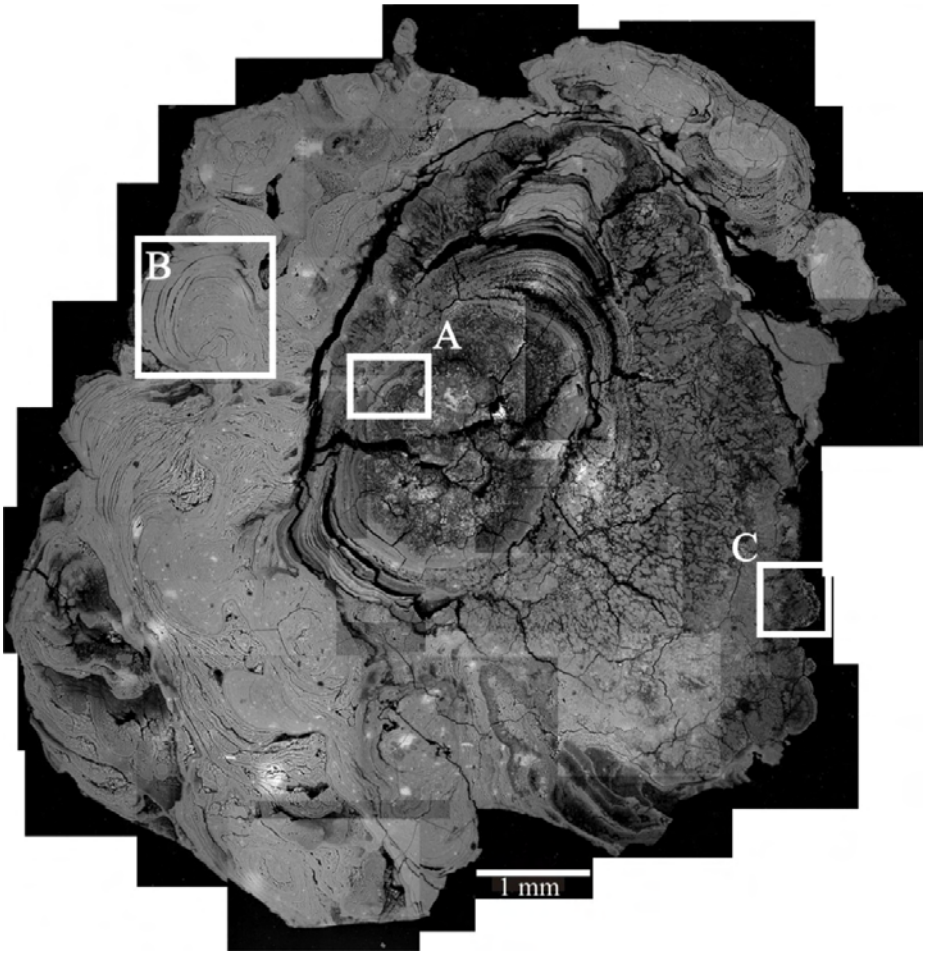

Figure 31. Sialolith 3 polished cross-section (BSE mode).

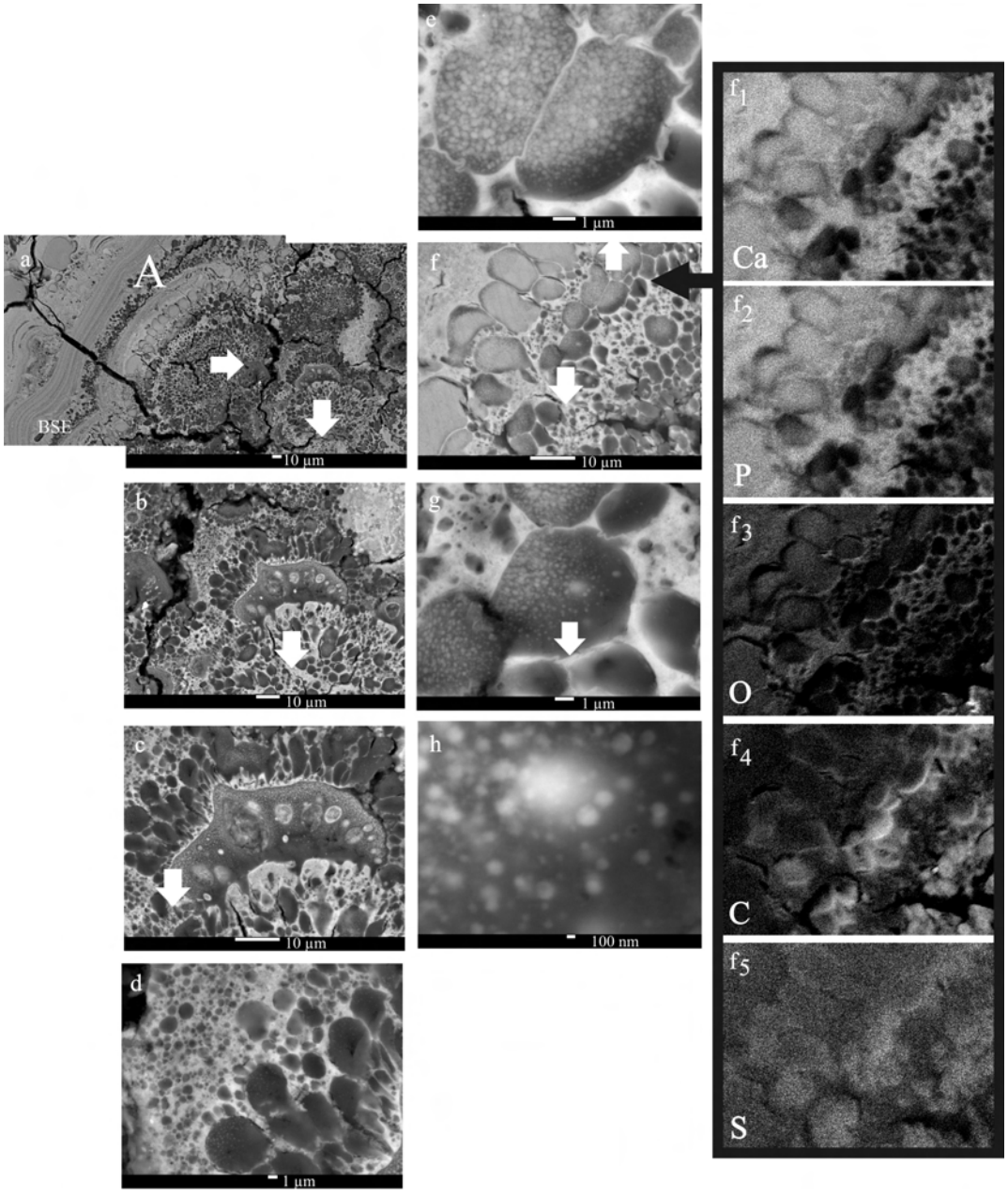

Figure 32. Detail A of sialolith 3 polished cross-section (BSE mode). The framed column on the right presents Ca, P, O, C and S X-ray maps of image (f).

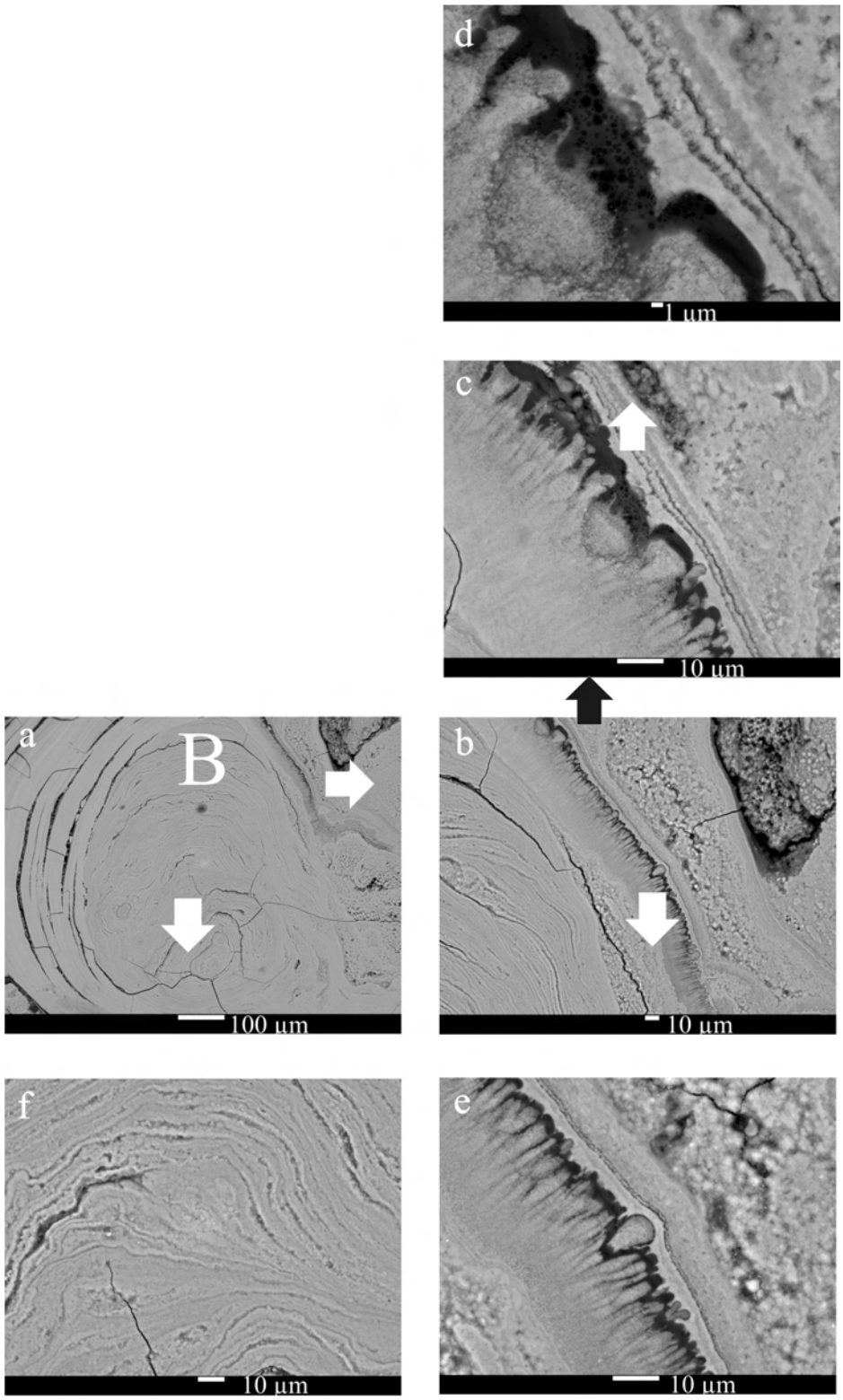

Figure 33. Detail B of sialolith 3 polished cross-section (BSE mode).

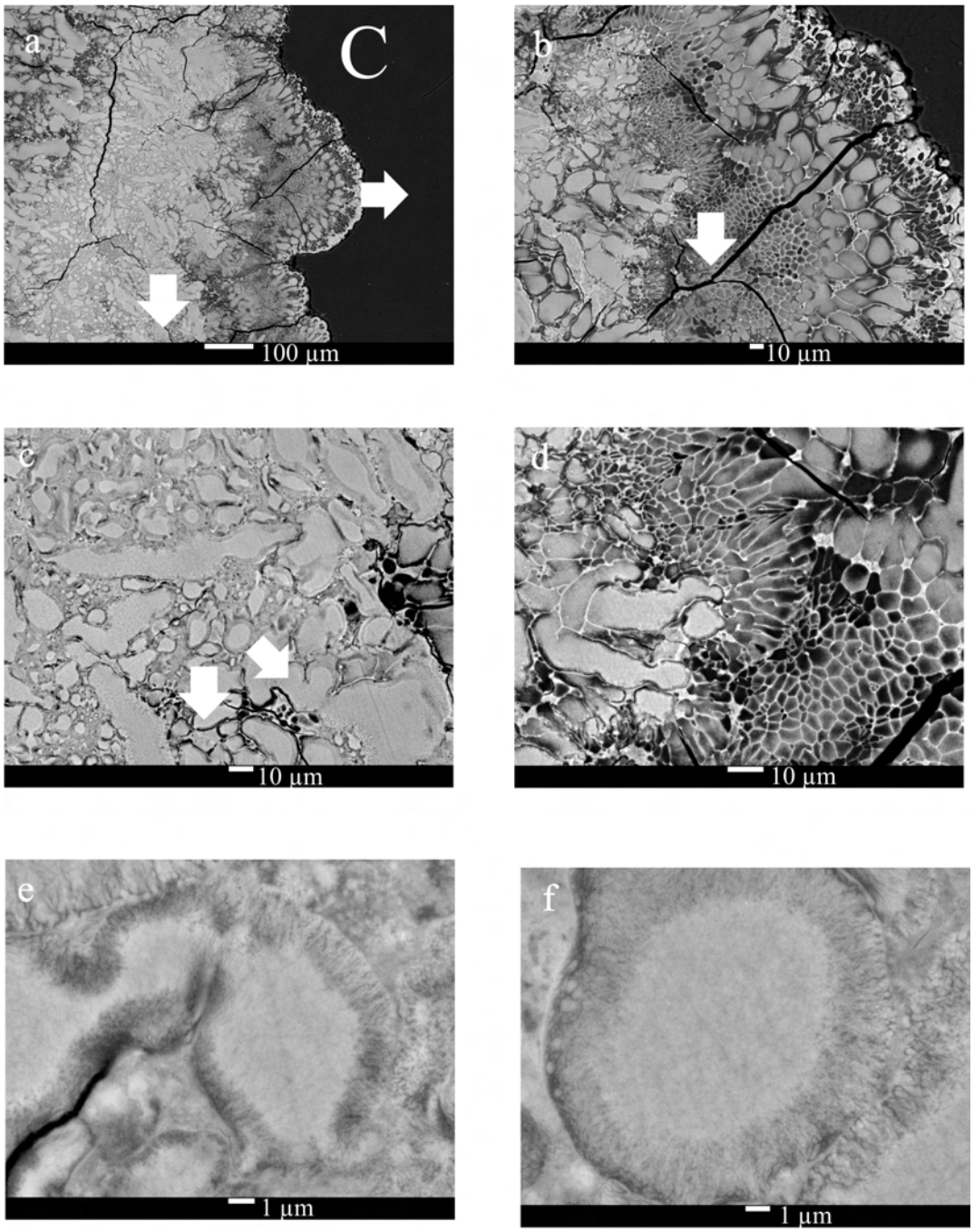

Figure 34. Detail C of sialolith 3 polished cross-section (BSE mode).

Sialolith 4

External morphology

Sialolith 4 presented a fairly regular conic shape with nearly 9 mm length and 5 mm diameter at the base (Figure 35). Overall, the calculus external surface was consistent and without cracks or apparent spalling. The base surface presented lower roughness than the conical surface, except for an irregular structure emerging at its centre (Figures 36 and 37).

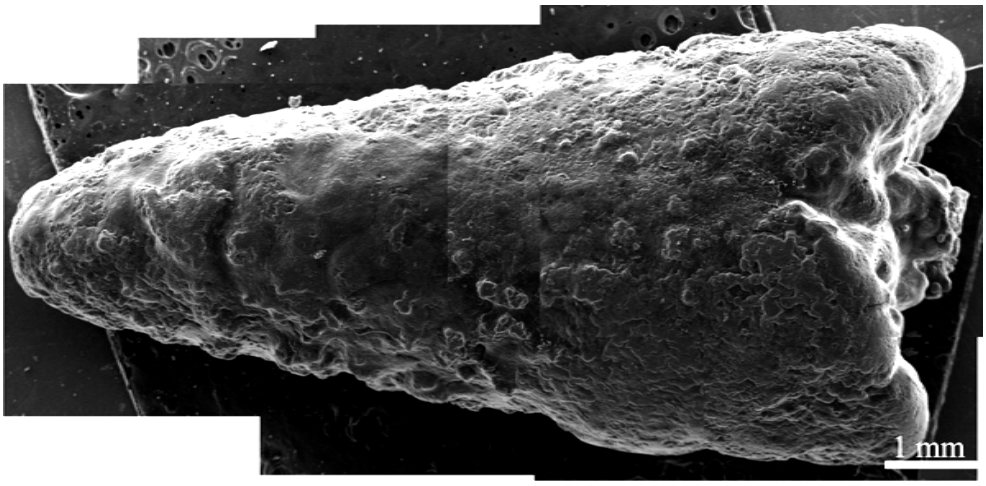

Figure 35. External surface of sialolith 4 (SE image).

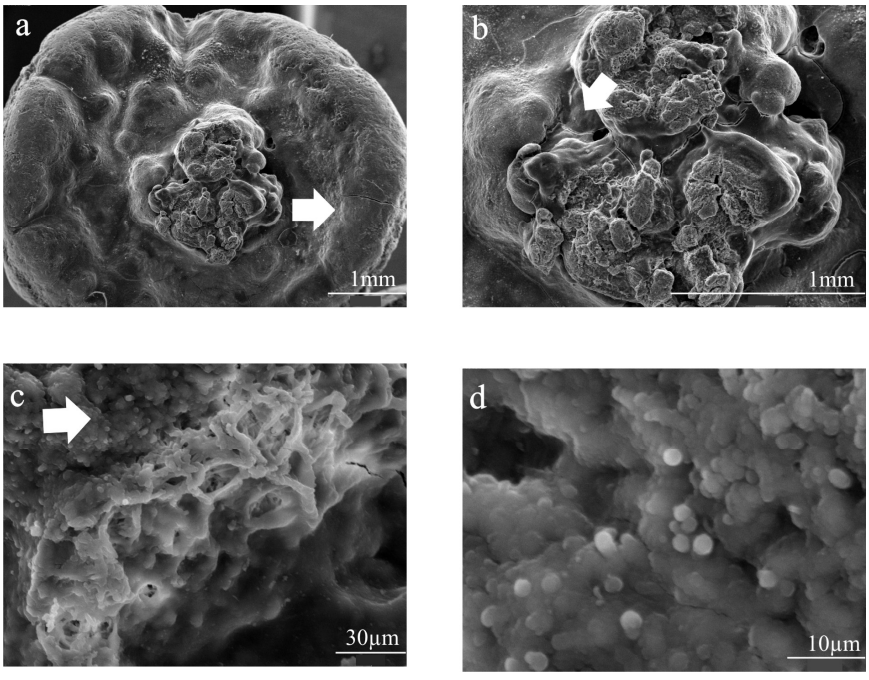

Figure 36. (a), (b and (c) Successive magnifications of the basal face of sialolith 4. (d) Nearby region where individual spherical particles of about 3 µm are clearly visible.

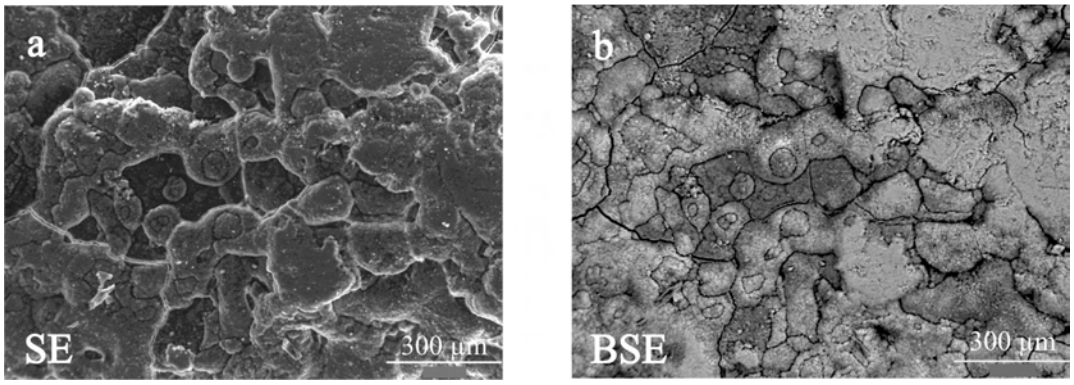

Figure 37. Lateral detail of the sialolith 4 external surface displaying a consistent appearance. (a) SE and (b) BSE modes, respectively.

Polished cross-section

Figure 38 exhibits the polished cross-section of sialolith 4. The calculus presents one central core with an irregular shape (where A,B and C details stand), loosely connected to the surrounding intermediate and nearly spherical layers (where D and E details stand), which in turn are loosely connected to the peripheral layers with a conical external shape (where F detail stands). These peripheral layers present a uniform structure and show a high mineralization contrast. The conical shape of the peripheral layers, which enclose the nearly spherical intermediate layers, indicates that at the latter growth stages the stone was forced to conform to the duct luminal shape.

A high concentration of globules surrounded by teardrop crescent structures could be found at the core (Figures 39 to 41). Calcification of the globules proceeded by agglomeration of Ca and P-rich flake structures (see for example, Figures 39 (e),(f), 40 (e),(f) and 41 (e),(f)). The intermediate layers displayed teardrop layers or collars (Figures 42 and 43) consisting of alternating bands of highly calcified globules and bands where globule calcification was still in course or was even incipient. In the intermediate region towards the uniform peripheral region, sequences of teardrop collars tended to reorganize into laminar layers (Figure 43 (b)). The peripheral layers presented a laminar structure (Figure 44).

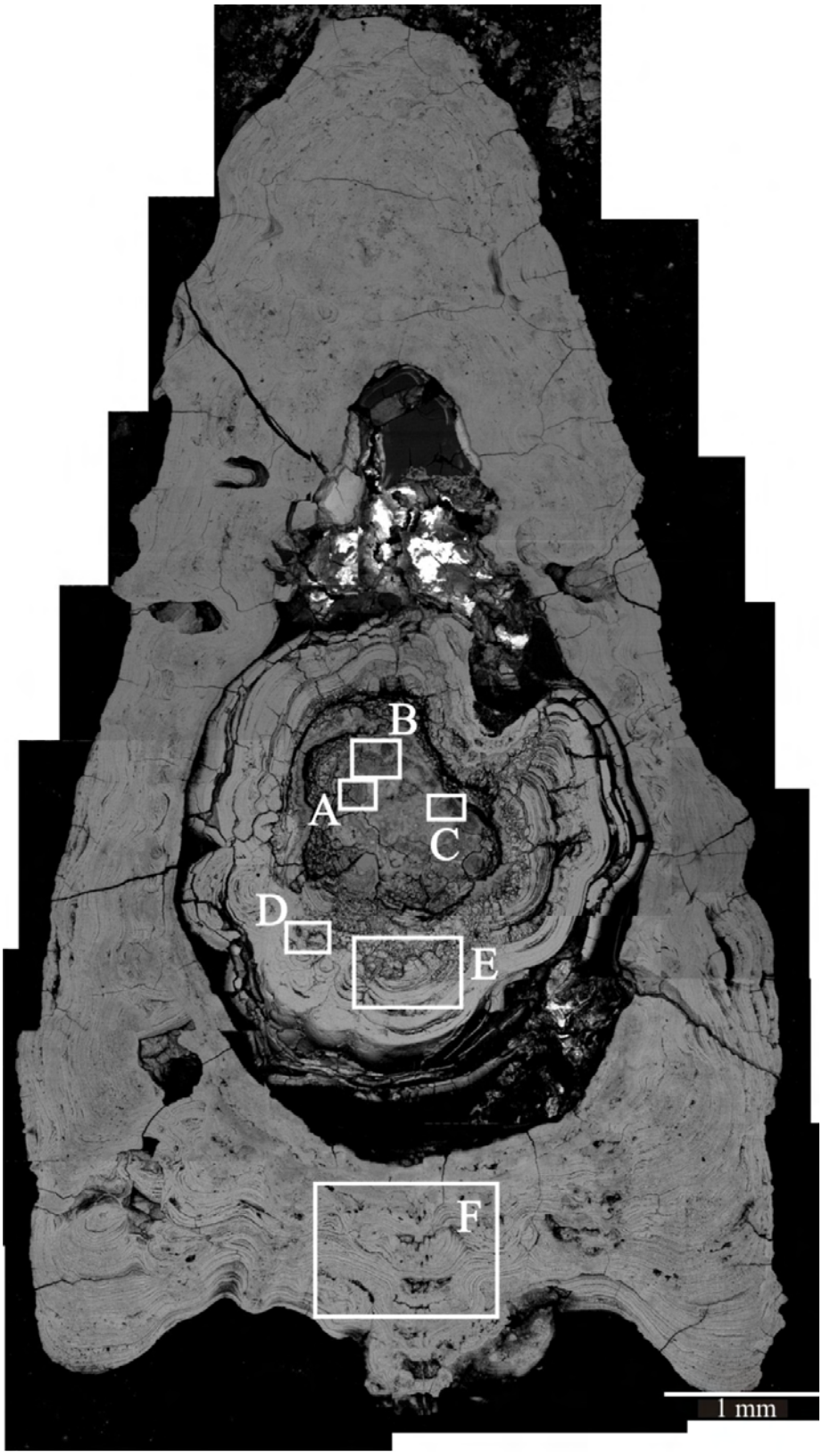

Figure 38. Sialolith 4 polished cross-section (BSE mode).

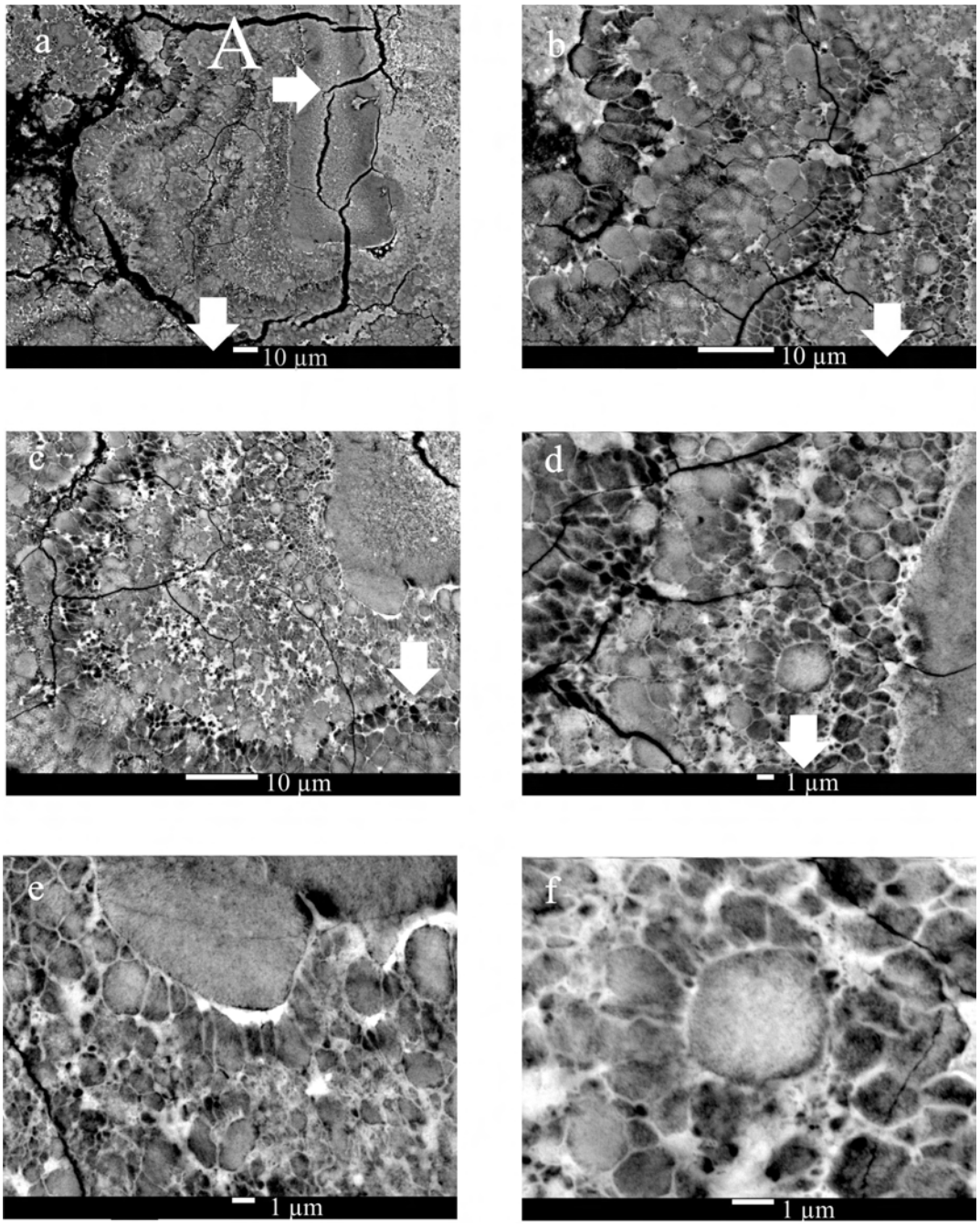

Figure 39. Detail A of Sialolith 3 polished cross-section (BSE mode).

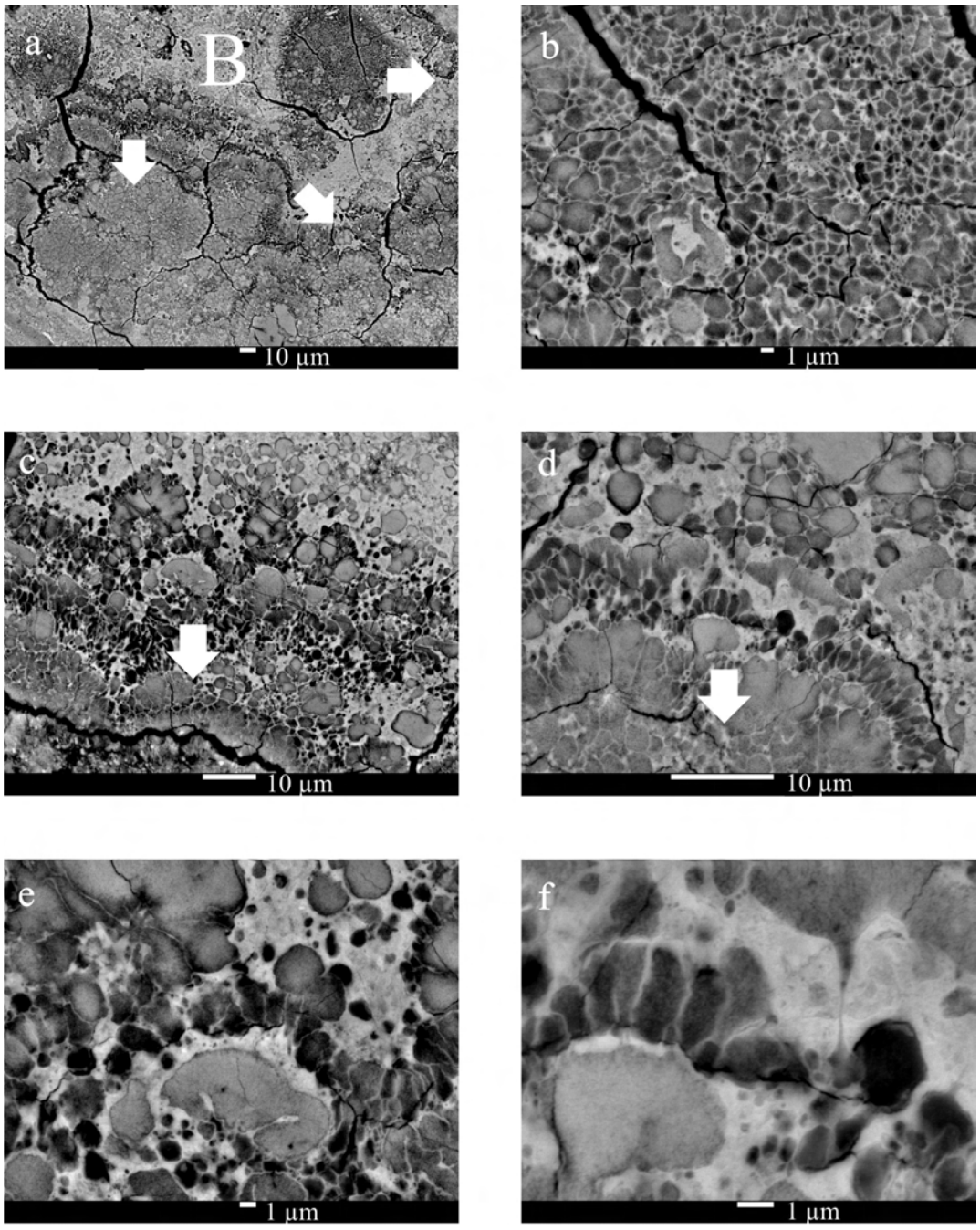

Figure 40. Detail B of sialolith 3 polished cross-section (BSE mode).

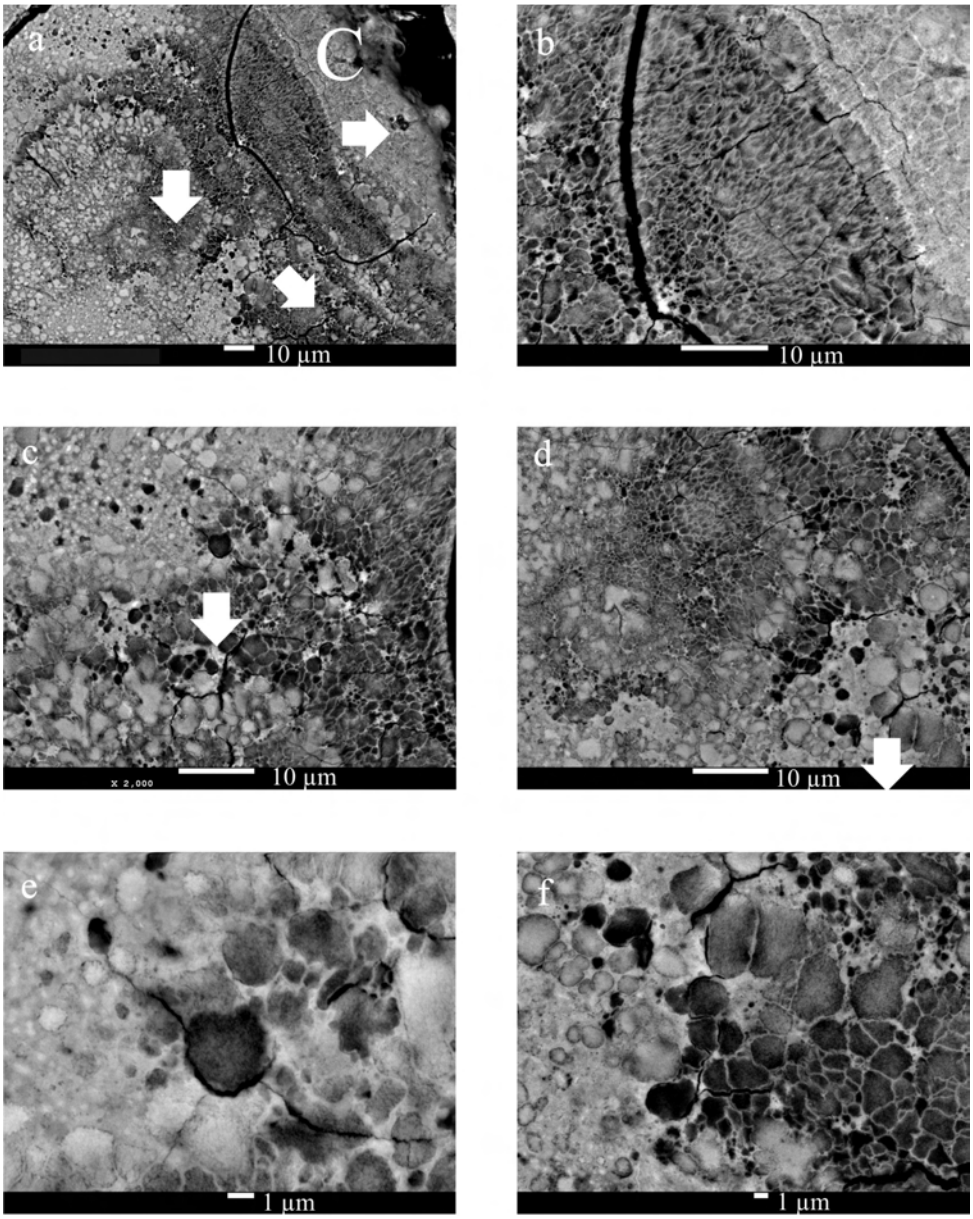

Figure 41. Detail C of sialolith 3 polished cross-section (BSE mode).

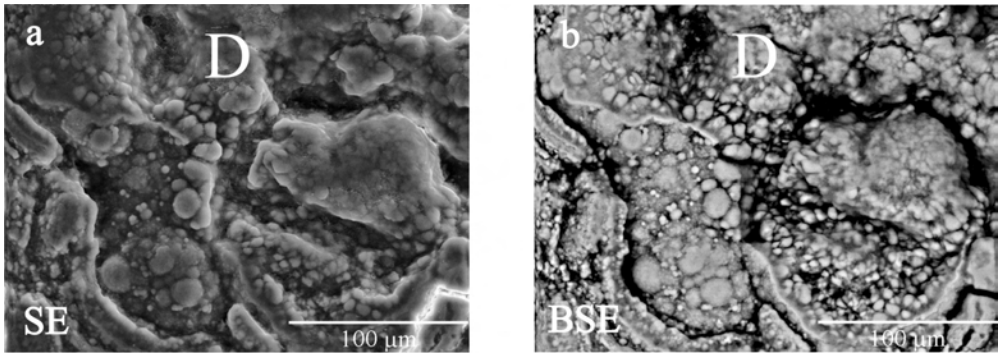

Figure 42. Detail D of sialolith 3 polished cross-section (BSE mode).

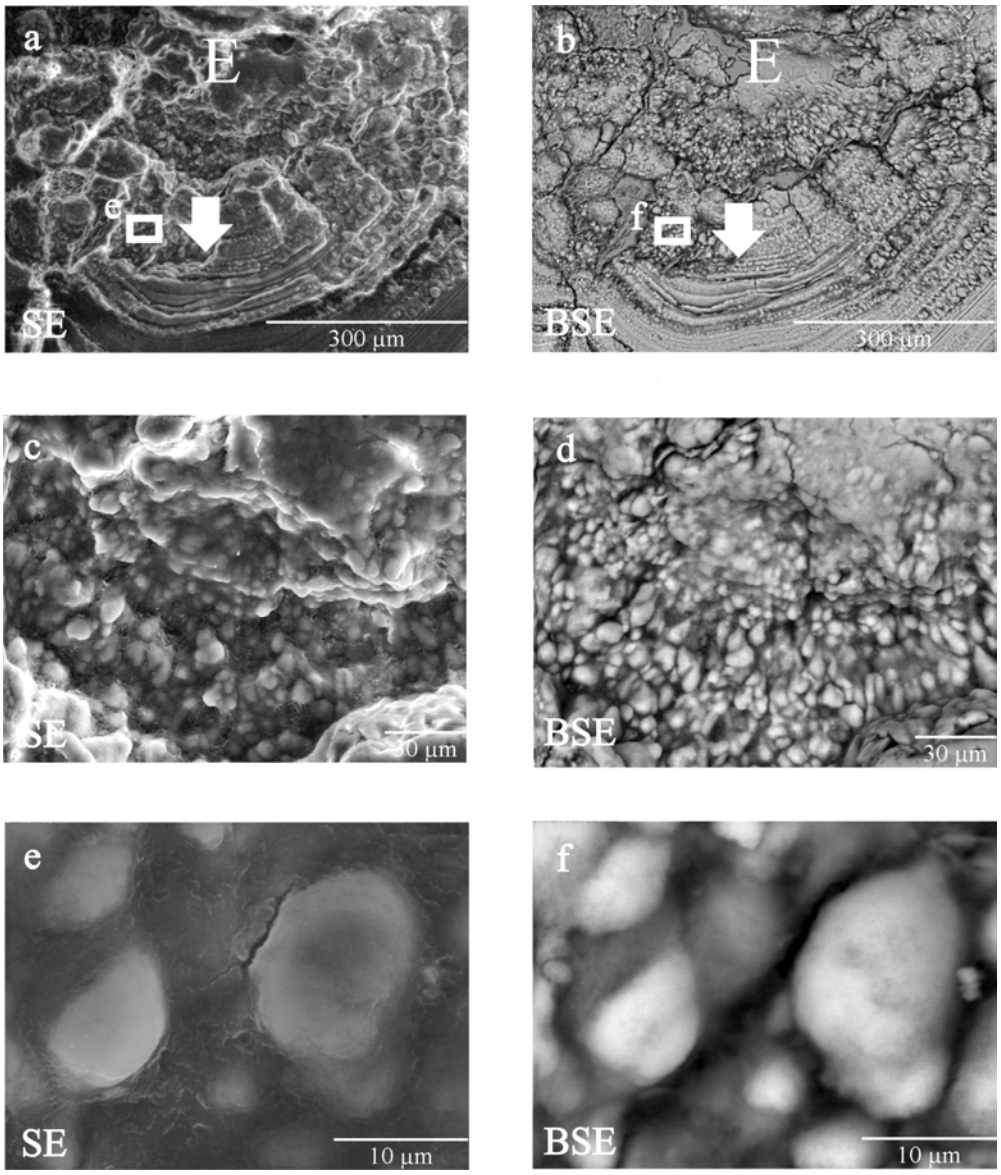

Figure 43. Detail E of sialolith 3 polished cross-section (left SE mode and right BSE mode)~.

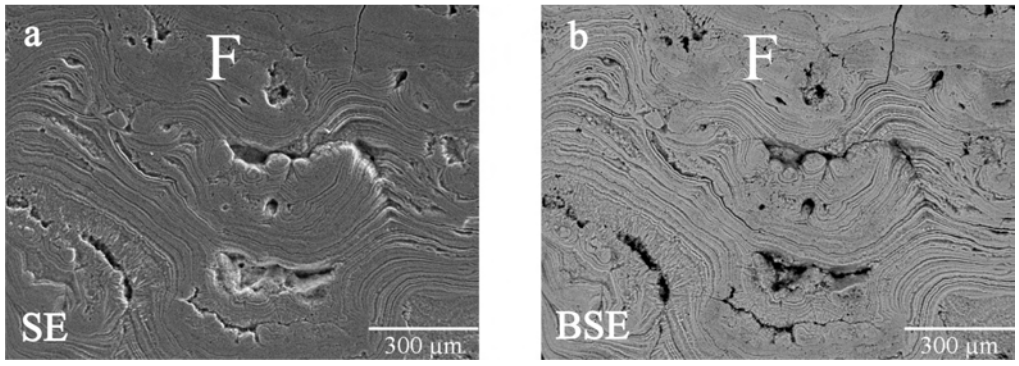

Figure 44. Detail E of sialolith 3 polished cross-section (left SE mode and right BSE mode).

Sialolith 5

External morphology

Sialolith 5 presented an irregular conical shape with approximately 11 mm of length and 7.5 mm of maximum diameter (Figure 45). The frontal region showed a surface with low roughness while the lateral regions presented bulges and a scale like appearance (Figures 46 and 47). Surface details shown in Figures 47 revealed that the spalled external organic layer (~20 μm) contained S and that the exposed internal zone was rich in Ca and P.

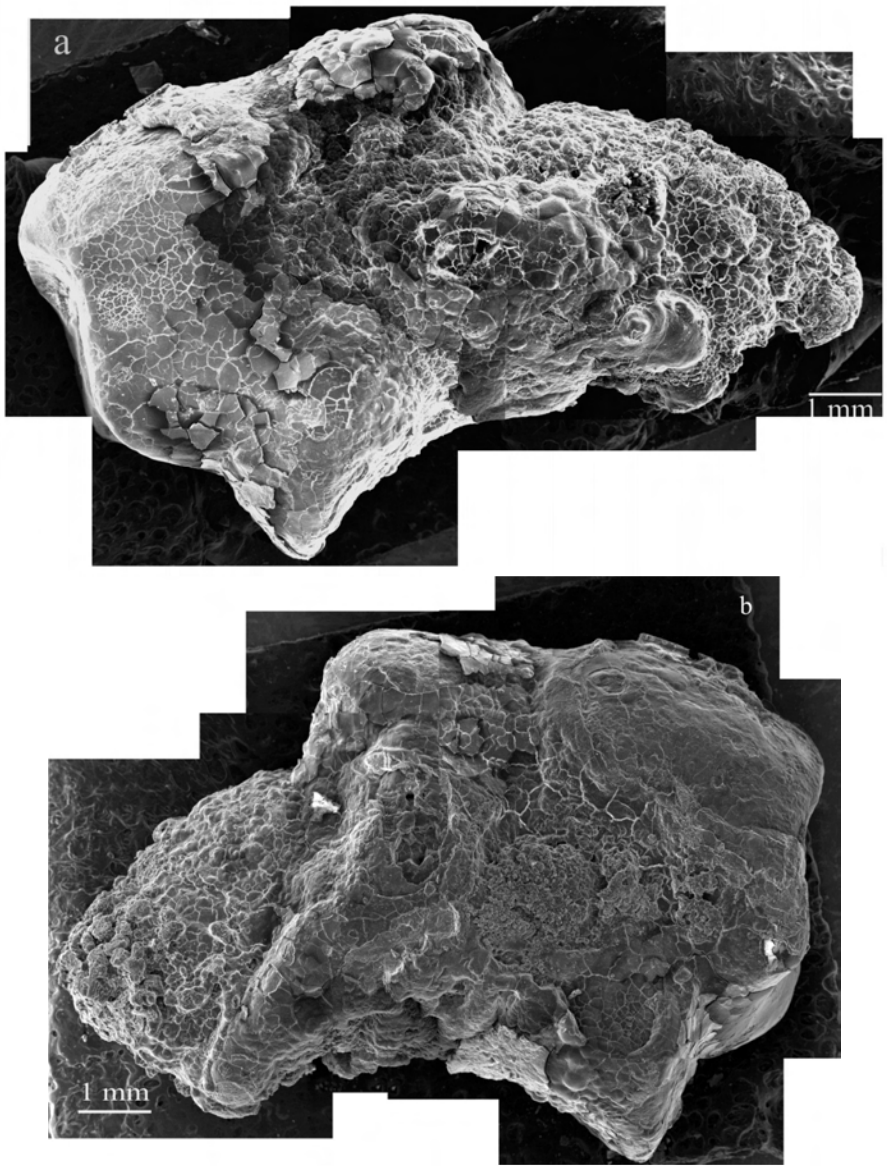

Figure 45. External surface of sialolith 5: side A (a) and side B (b) (SE mode).

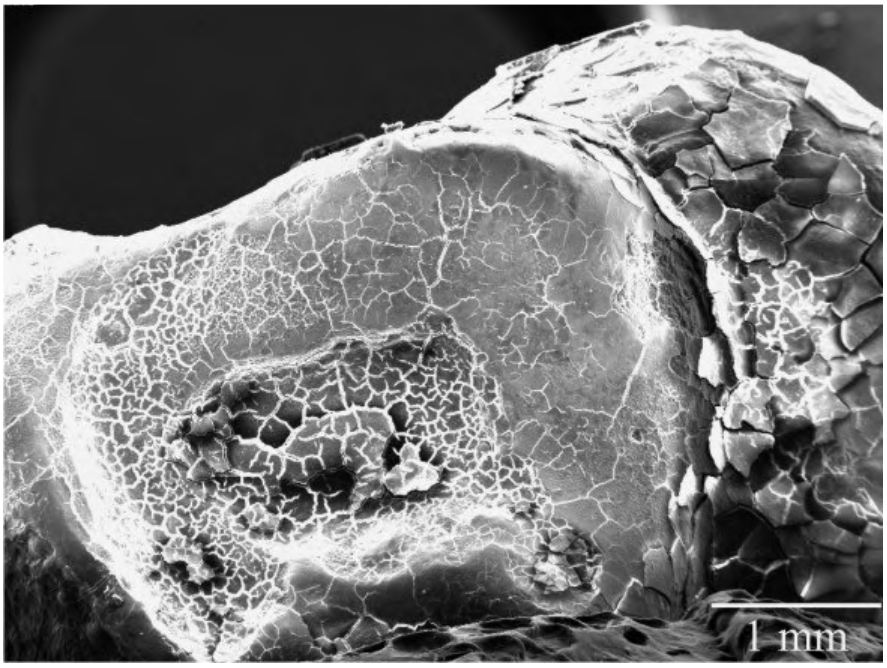

Figure 46. Frontal view of sialolith 5 (SE mode).

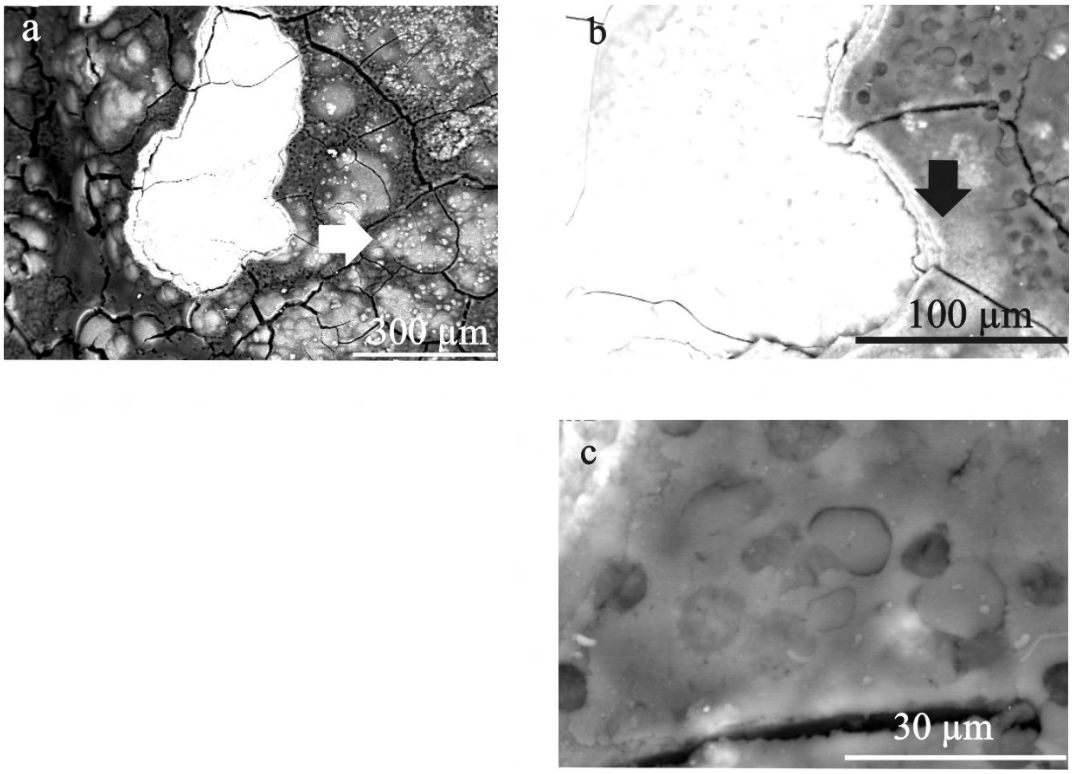

Figure 47. Surface details of sialolith 5. under BSE mode. (b) is a magnified detail of (a) and (c) a magnified detail of (b) (BSE mode). Brighter contrast evidences higher average atomic weight. EDS analysis revealed a high content of Ca and P in the bright regions. The darker regions contain S.

Fracture Surface

The fracture surface of sialolith 5 shown in Figure 48 revealed that the central core consisted in aggregates of mineralized spheres with ~10 µm diameter.

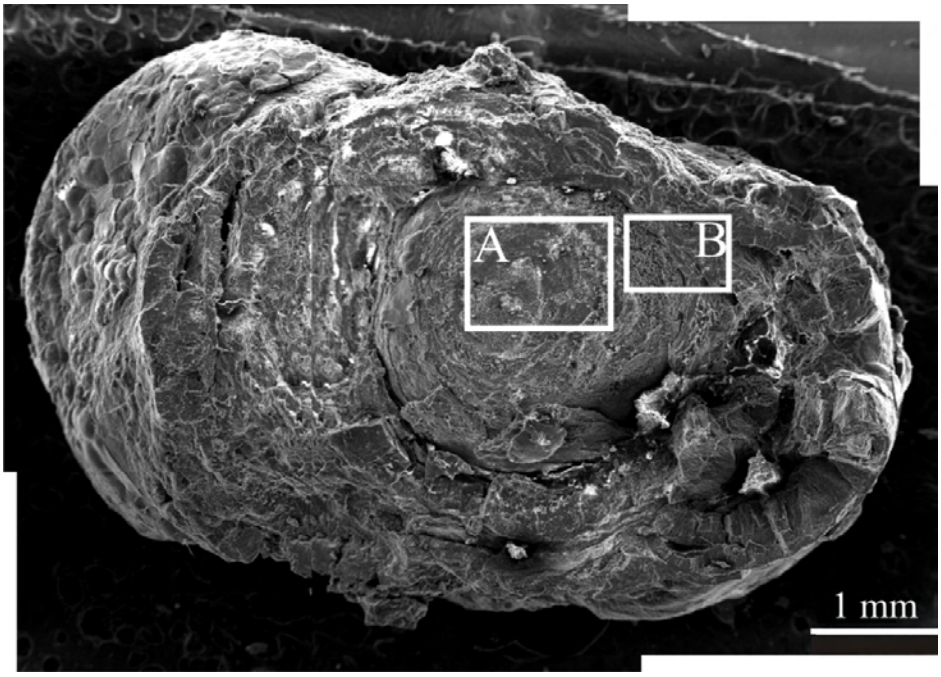

Figure 48. Fracture surface of sialolith 5 (SE mode).

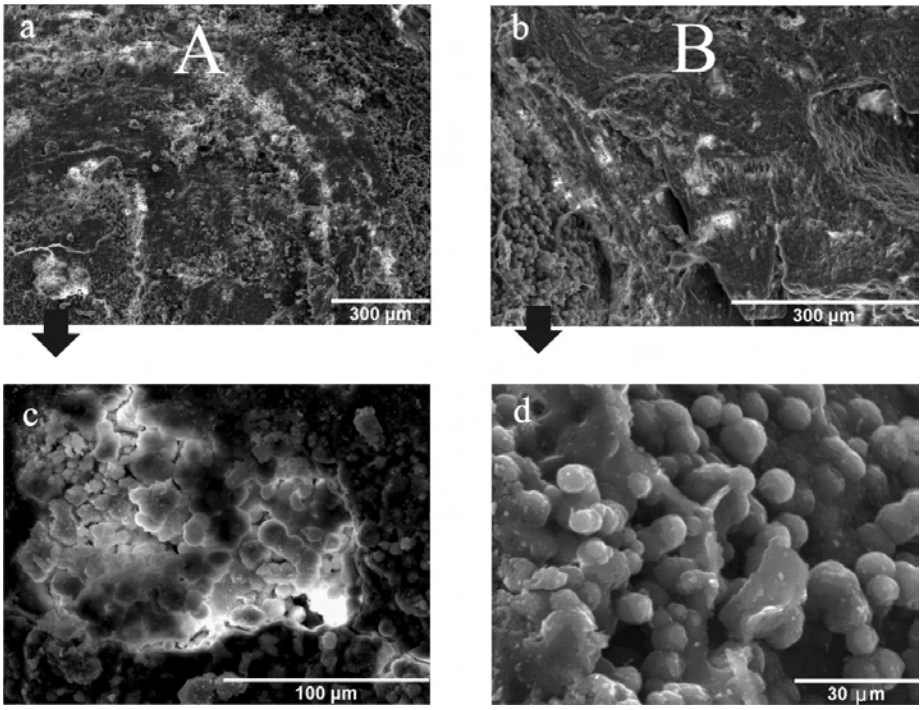

Figure 49. Magnified details A and B of the fracture surface of sialolith 5.

Polished cross-section

Figure 50 shows the general appearance of the polished cross-section of sialolith 5. During sample preparation the central core detached and was lost. The absent core presented an approximately spherical shape and was evidently loosely connected to the encasing laminar layer, which displays an extremely regular structure and an approximately spherical shape. Two other major regions can be distinguished in the image: a subsequent region with teardrop globular collars exhibiting heterogeneous mineralization and a following laminar region. The overall shape of these two last regions suggests a conformation to the duct lumen or gland shape.

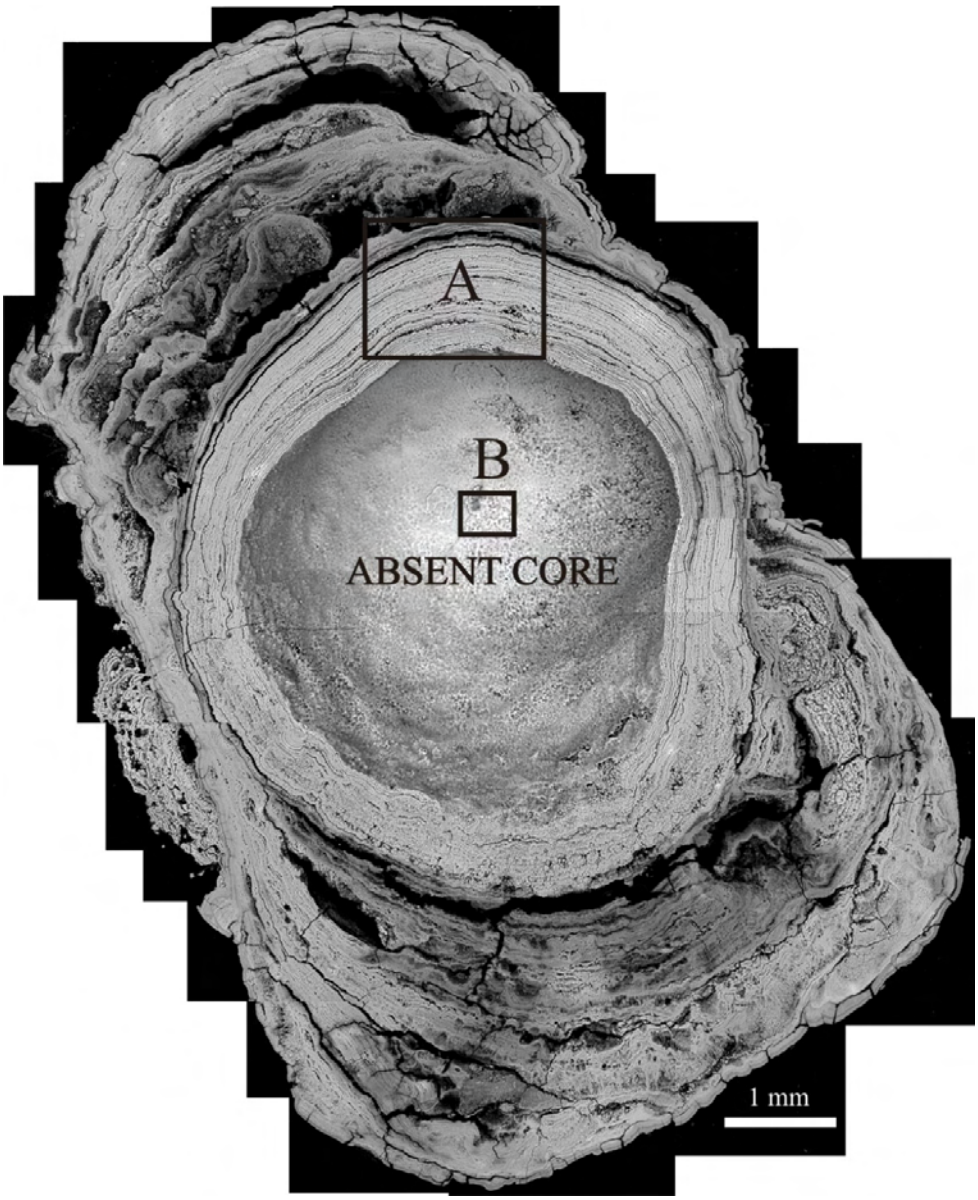

Figure 50. Sialolith 5 polished cross-section (BSE mode).

Detailed inspection of the polished cross-section revealed that the regular laminar layers around the core consisted of highly mineralized thin strata (bright under BSE mode) with ~5 μm of thickness intercalated with organic (darker) strata (Figure 51). Strata composed by mineralized spheres could also be observed towards the core region.

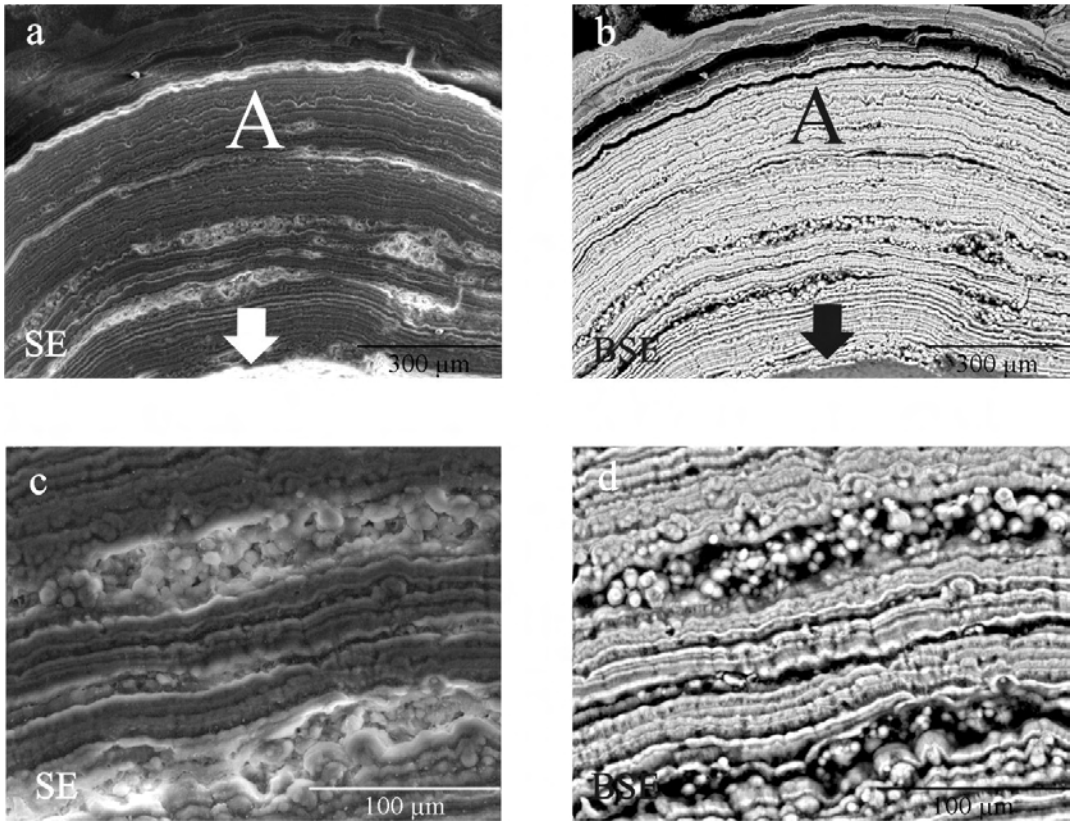

Figure 51. (a) SE and (b) BSE images of detail A in Figure 50.

The free surface underneath the (absent) core displays a high density of mineralized spheres, with sizes ranging from 5 to 20 μm, encased in a matrix presenting a lower level of mineralization (Figures 52 and 53). Some zones of the fracture surface show features that are characteristic of a ductile material containing hard inclusions (Figure 53 (c) and (d)) [26,27].

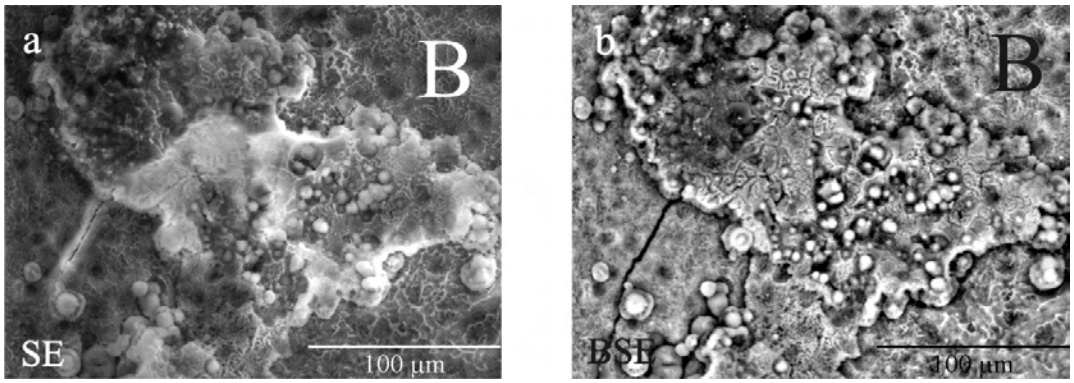

Figure 52. (a) SE and (b) BSE images of detail B in Figure 50. The mineralized spheres range for 5 to 20 µm in diameter.

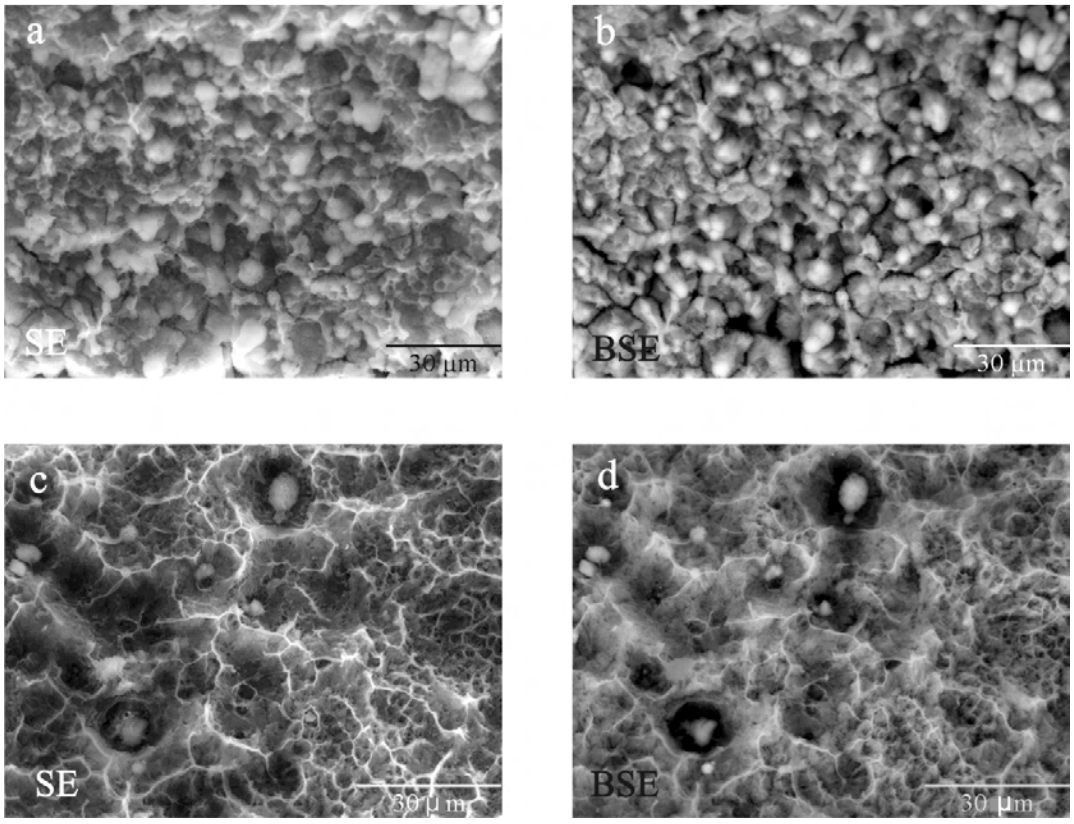

Figure 53. (a) and (c) SE images and corresponding (b) and (d) BSE images of the region below the nucleus (absent) in Figure 50.

3.2 Attenuated Total Reflection - Fourier Transform Infrared spectroscopy

Figure 54 shows ATR-FTIR spectra obtained from the polished cross-section of sialolith 3 in the 4000 to 650 cm^{-1} range.

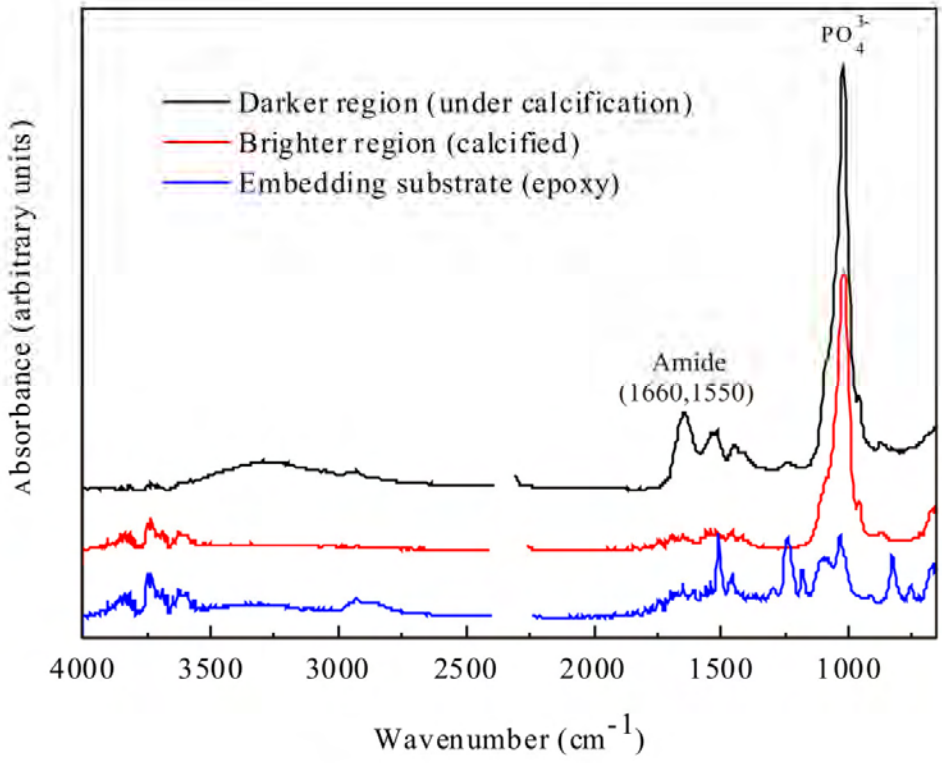

Figure 54. ATR FT-IR spectra of polished surface of sialolith 3. The spectra were collected at the central darker region, at the peripheral brighter region and at the embedding substrate.

The spectra exhibit characteristic peaks within the fingerprint region of 1500-600 cm^{-1} attributed to the vibration of phosphate and carbonate in the hydroxyapatite structure: CO_3 ν_3 located at ~1410 cm^{-1}, CO_3 ν_3 ν_2 at ~880 cm^{-1}, and $PO_4^{3-}\nu_3$ and $PO_4^{3-}\nu_1$ at ~1014 and ~960 cm^{-1}, respectively [30]. The strong signal due to the PO_4 ν_3 band is more intense in the bright peripheral region of the sialolith.

The spectrum obtained at the least mineralized region exhibits bands characteristic of amide groups present in proteins and polypeptides, namely collagen. The band at ~1660 cm^{-1} corresponds to the absorption of amide I group, which results from a combined vibration of C=O stretching with C-N stretching and N-H bending modes, and

may indicate that the secondary structure of collagen exists under an α-helix form. The absorption band at ~1550 cm^{-1} corresponds to N-H bending coupled to C-N stretching in amide II, and is also characteristic of collagen [28,29].

The vibrations of the phosphate and carbonate groups as well as the amide I and II bands in the ATR-FTIR spectra enable to infer that: (i) the inorganic matter of the sialolith corresponds essentially to calcium phosphate and calcium carbonate in the hydroxyapatite form; (ii) the organic matter of the sialolith corresponds probably to collagen; (iii) the concentration of hydroxyapatite is higher at the bright peripheral layers.

3.3 Nuclear Magnetic Resonance Spectroscopy

Figure 55 shows the ^{13}C-nmr spectra of powdered sialoliths 6 and 7 obtained by the cross-polarization-magic-angle-spinning (CP-MAS) method.

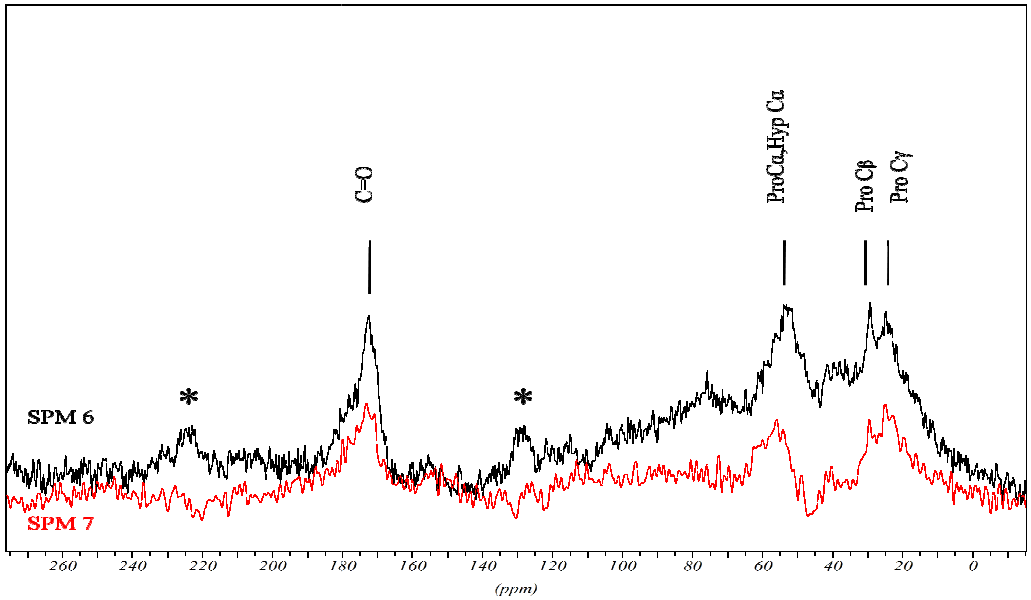

Figure 55. ^{13}C-MAS spectra obtained with a spinning rate of 4 kHz and a contact time of 2 ms from powdered sialoliths 6 and 7. The marker * indicates spinning side bands

The spectra although complex contain three major sets of chemical shifts at ~173, ~56 and ~25 ppm, which are in agreement with collagen-like polypeptides [24,26]. The two broad signals near 25 ppm can be attributed to Pro C_β and Pro Cγ, while the broad signal at 56 ppm can be assigned to Hyp C_α and Pro C_α. The signal at

173 ppm results from C=O. The width of these peaks in collagen ^{13}C -nmr signals is a measure of the denaturation degree [33,35]. Since the powdering process is not expected to affect the structure of proteins present in the samples [34], the denatured collagen present resulted from the salivary calculus formation itself. Sialolith 6 produced a higher background due to the carbon coating required for SEM observations, which was not used with sialolith 7.

The chemical shifts observed correspond therefore to amino acid residues that indicate the presence of denatured collagen [33,35].

3.4 Atomic Force Microscopy

3.4.1 Lateral force microscopy

Figure 57 shows the topographic (a) and LFM (b) images obtained at the polished cross-section of sialolith 3 in an area previously selected through BSE mode observation (Figure 56). As it can be observed in Figure 57 (b), the weakly mineralized globules (and even the teardrop crescents at the top of the left globule) present darker LFM contrast and therefore correspond to a lower friction coefficient.

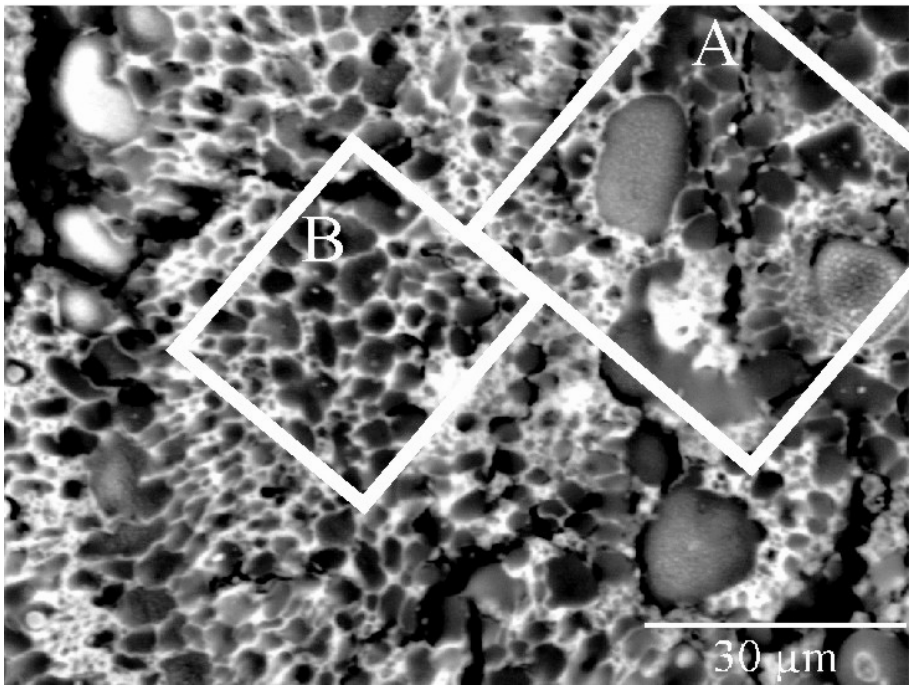

Figure 56. Globular region at the core of sialolith 3 (polished cross-section, BSE mode).

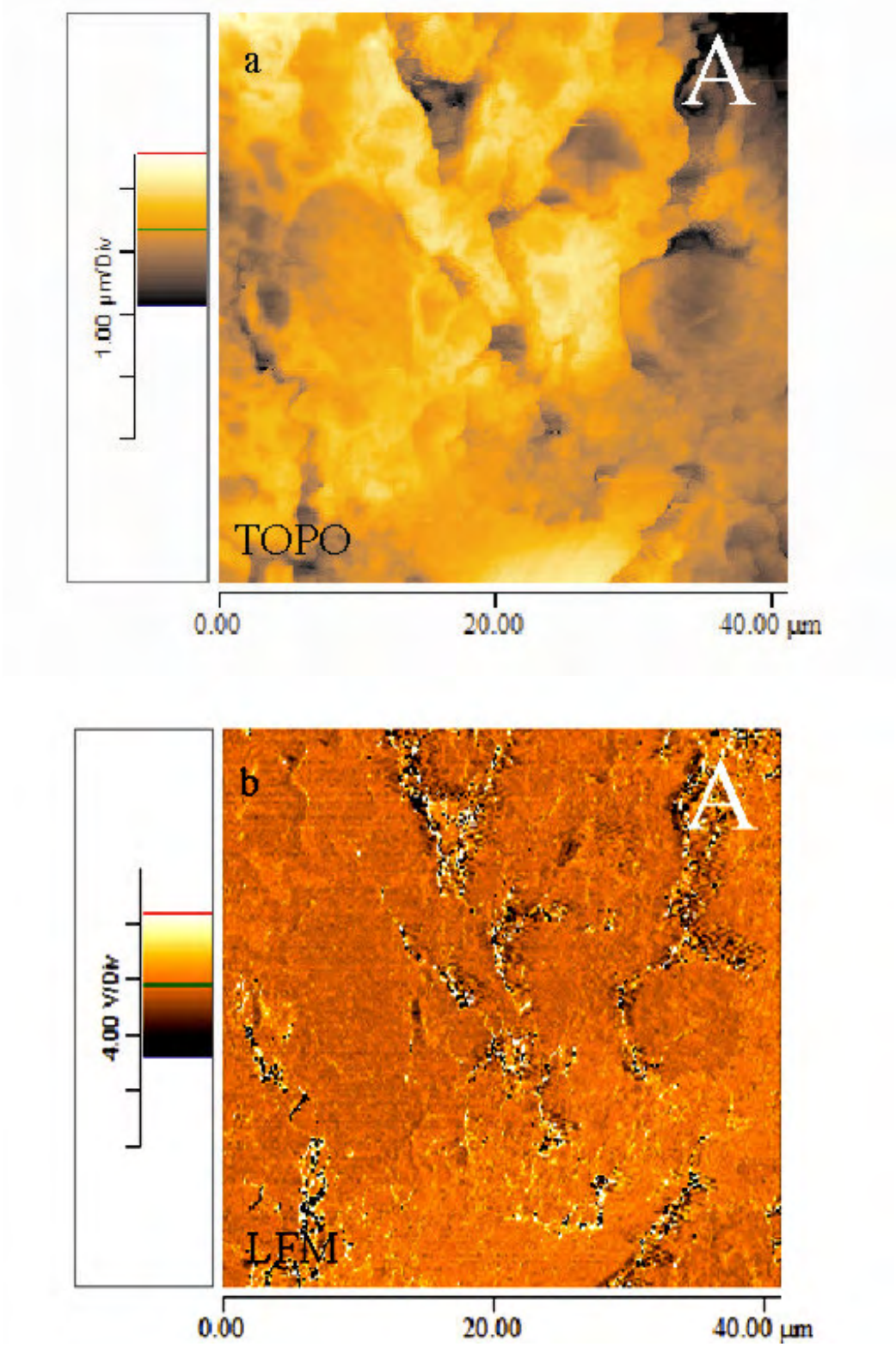

Figure 57. (a) Topographic and (b) friction images from polished cross-section A in figure 56 (scan size: 41.15µmx41.15µm). Darker areas in (b) represent lower friction.

3.4.2 Force spectroscopy (FS)

Figure 58 shows typical force-distance curves obtained in distinct points of sialolith 3 polished cross-section. The force plots were obtained through indentation of a weakly mineralized globule (a) and a region with higher mineralization level (b). The hysteretic behavior of the tip-sample interaction can be used to compare the relative work of adhesion. In fact, although a quantitative measure of adhesion forces requires vacuum, since both curves were obtained under identical conditions, the results can be qualitatively compared: the area enclosed in the force loop, which represents the work done in the approach-retract cycle by the tip-sample interaction [36], is in Figure 58 (a) approximately the triple of the one in Figure 58 (b). On the other hand, the approximately constant slope shows that the Young Modulus is similar for both regions.

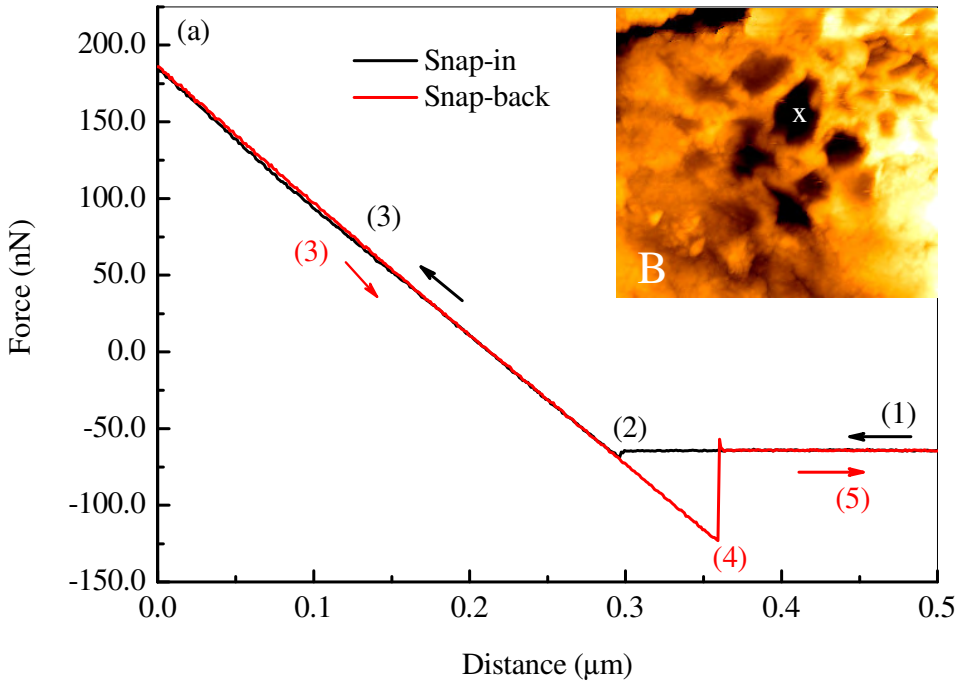

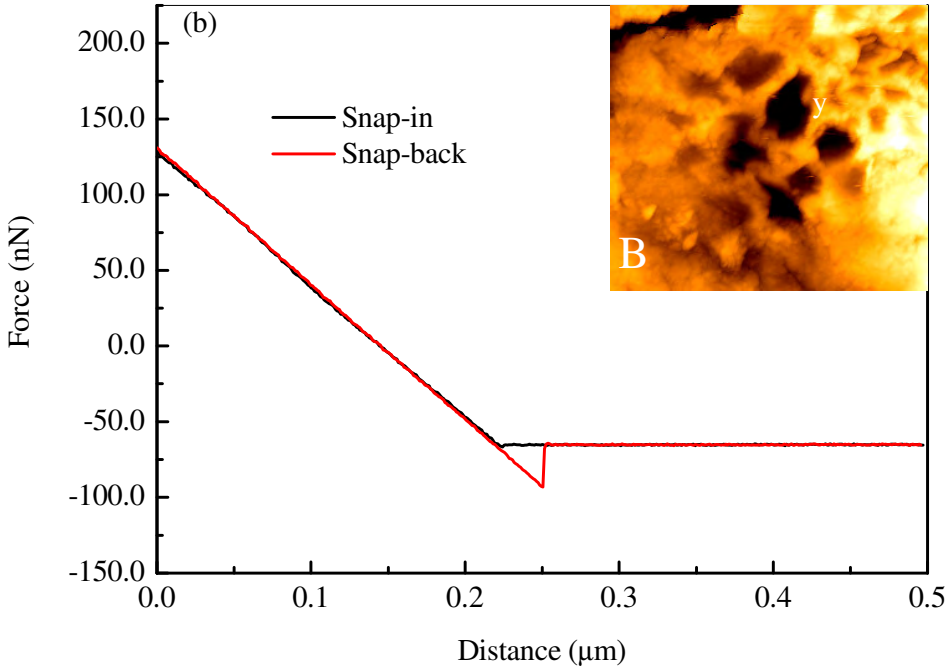

Figure 58. Force-distance curves obtained at the points indicated at AFM image insets (scan size: 23.52µmx23.52 µm). (a) point x is located in a weakly mineralized globule, (b) point y is located in a region with a higher mineralization degree. Different stages of a force-distance curve are indicated in (a): (1) tip far from the surface sample and the long range interactions are too small to give measurable deflections; (2) tip close enough to the sample surface for attractive forces (Van der Waals, capillarity) to overcome the cantilever spring constant, so the tip makes a discontinuous jump to contact; (3) tip in contact with the surface, the distance between the base of the cantilever and the sample continues to decrease causing deflection of the cantilever and an increase of repulsive forces, defection is gradually released when the tip is slowly retracted; (4) tip effectively loses contact with the surface while the cantilever is still deflected downwards due to adhesive forces; (5) tip far away from the sample and the cantilever is no longer influenced by tip-sample interactions.

4 Discussion and Proposed Mechanisms

4 Discussion and Proposed Mechanisms

Although the specimens investigated present dimensional, morphological and structural diversity some common or typical features can be summarized as follows:

- Typically each salivary calculus exhibits one core with irregular shape. The core evidences organic globular structures partially or highly mineralized and is loosely connected to the subsequent layers. Exclusively organic cores, clearly identifiable foreign bodies or microorganism-dependent structures have *not* been detected.
- The subsequent layers present either laminar or globular structures. These layer types alternate thereafter in succession following a chronologic sequence. Sialoliths 2a) and 5 are examples of the core → laminar→ globular sequence, while sialoliths 1 and 4 are examples of the core → globular → laminar sequence.
- Laminar layers consist of fine mineralized strata (1-10 μm) intercalated with fine organic strata (1-5 μm), which points to a sedimentary growth mechanism similar to the one described for renal calculus [39,40].
- Globule size ranges from 500 nm to 50 μm. Typical 3-D globule morphologies are close to teardrop shapes, with nearly circular configurations in transverse cross-sections and elongated configurations in longitudinal cross-sections.
- Globular layers or collars consist of alternating bands of highly calcified globules and bands where globule calcification was still in course or was even incipient.
- Mineralizing globules are surrounded by teardrop globule crescents also partially mineralized. These structures result clearly from a "squeezing process" induced by pressure buildup and indicate organic matter replacement inside the globules. Successive squeezing processes form fractal-like patterns (e.g. Figure 32 (b,c,d).
- The organic matter in the globular structures and organic strata presents a high concentration of denaturated collagen, probably originating from fibroblast cell invasion and connective tissue formation in the sialolith precursor structures.
- Mineral matter in the sialoliths consists essentially of hydroxyapatite.
- Mineralization of organic globular structures proceeds by diffusion of Ca and P to the globule interior, followed by precipitation of mineralized flakes, which grow or agglomerate inside the globules and transform during the process into hydroxyapatite. Both centre → outwards (Figure 9 (c)) and periphery → inwards (eg. Figure 34 (d) and [16] globule mineralization have been detected.

In view of the observations a mechanism for sialolith formation is proposed in Figure 59 based on the following stages:

(1) Initial foreign body or luminal organic nidus formation.

(2) Fretting of foreign body/nidus damages duct/gland epithelial cells.

(3) Damage of duct/gland walls exposes the foreign body/nidus to connective tissue. Inflammation can be expected to be associated with this process. Bacterial infection may develop in the damaged tissue and may contribute to the calculus precursor structures.

(4,5) Connective tissue invasion of foreign body/nidus with extensive formation of collagen.

(6) Detachment of the invaded foreign body/nidus interrupts vascularization of the living connective tissue.

(7) Necrosis follows.

(8) Reorganization of the decayed organic molecules and mineralization

The structures resulting from stage (2) to (8) are globular. Alternatively, sialolith growth can proceed by sedimentary precipitation of highly mineralized strata intercalated with thin organic layers through a sedimentary cycle (9).

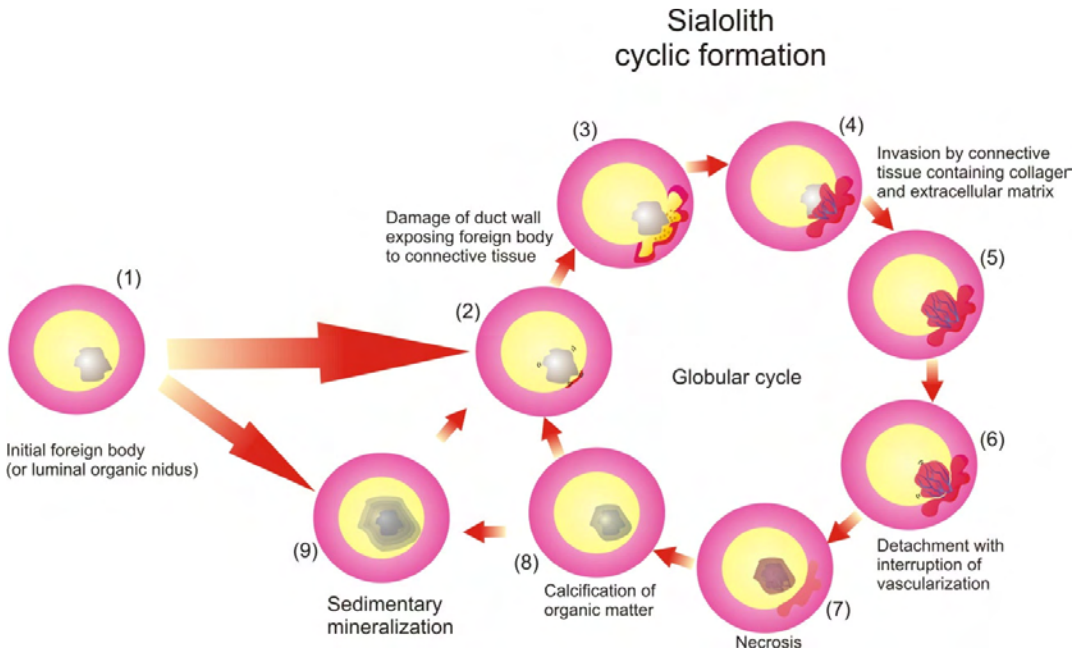

Figure 59. Schematic drawing representing the globular and sedimentary cycles of sialolith formation.

Evidence supporting the globular cycle proposed in stages (2) to (8) is visible in Figure 31, where a globular core, partially surrounded by intermediate laminar layers, appears encased by a globular pedunculus (indicated in Figure 60). The partially mineralized pedunculus may have been originally connected to the duct/gland wall and caused growth asymmetry on the subsequent laminar layers.

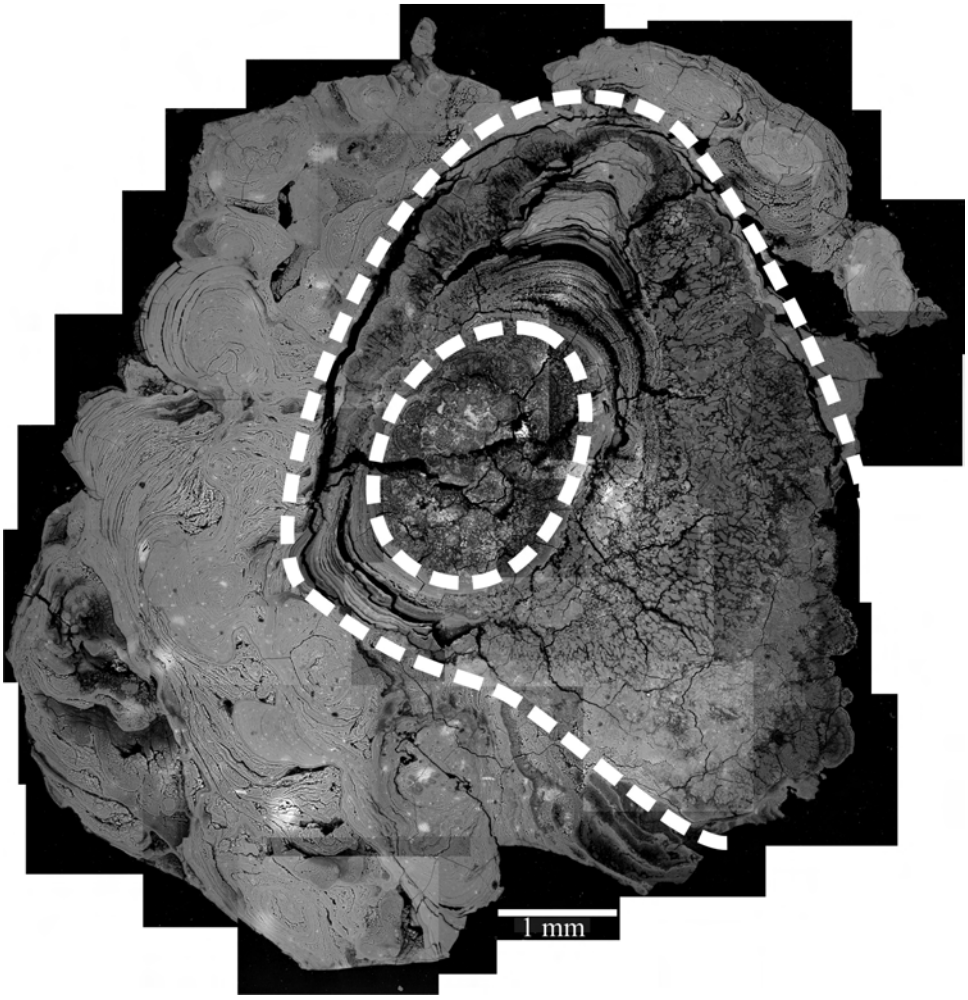

Figure 60. Indication of globular core and of encasing globular pedunculus, which appears to have been connected to the duct/gland wall (compare with Figure 31).

The sedimentary cycle (9) may never take place [16]. Alternatively, the foreign body/nidus formation stage may be directly followed by a sedimentary cycle and the globular cycle may never occur or occur subsequently. Nonetheless, the most frequent

sequence seems to be: foreign body/nidus formation → globular mechanism→ sedimentary mineralization → globular mechanism → sedimentary cycle…

The proposed mechanism suggests that during stages (2) to (4) inflammation of the duct/gland (and possible bacterial infection) may happen, whereas dull inflammation or even asymptomatic growth may be produced during sedimentary stage (9) to which minimal wall damage seems associated. Controlled follow-up of the sialolith clinical evolution and regular radiographic measurements would allow establishing a chronological scale for the layer sequence.

Regarding the mechanical properties, the AFM investigation demonstrated that although both organic and mineralized regions exhibit similar Young modulus, the work of adhesion to a silicon tip is significantly higher in organic regions. Furthermore, some zones showed a fracture surface characteristic of a ductile material containing hard inclusions. Ductile fracture is preceded by substantial plastic deformation. Hence when a material contains relatively hard inclusions which do not deform at the same rate as the matrix, voids are nucleated to accommodate this incompatibility. The nucleation event typically involves decohesion at the inclusion-matrix interface [26]. Overall macroscopic fracture occurs when voids nucleated from different inclusions have grown sufficiently to link up. This is illustrated in Figure 61. When a ductile-fracture surface is examined, the appearance is of 'dimples', with each dimple corresponding to a void. It is frequently possible to observe the inclusion responsible for nucleating the void within the depth of the dimple (see Figure 53 (c)).

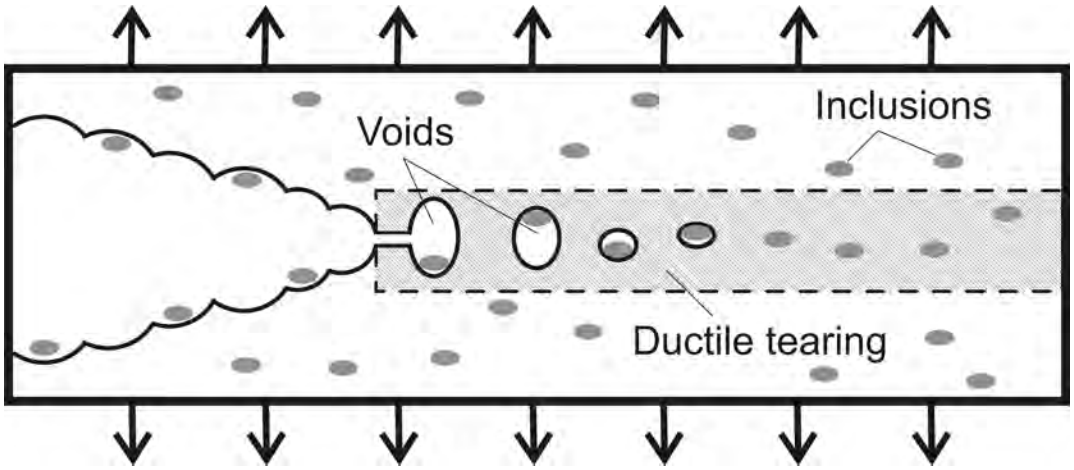

Figure 61. Diagram representing the fracture of a ductile material with hard inclusions [27].

The relatively high work of adhesion and the ductile behavior observed may justify the modest success rates obtained by shock wave lithotripsy with salivary calculi [19-24], when compared for example with renal calculi [37] which contain less organic material [38].

As with most research works the present study elucidates relevant mechanisms but raises additional issues, namely:

- What organic molecules promote mineralization? What is their role in Ca and P diffusion? What is their effect in flake formation? Is S associated with these molecules?
- Is the globular morphology induced by physical processes? Indeed, an initial segregation between the phase rich in denatured collagen and the hydroxyapatite-rich phase (or its precursor structure) is apparent (e.g. Figure 25). Furthermore, the morphology adopted by the collagen-rich phase suggests a gel-like deformable behavior compatible with interfacial energy minimization in the system. Or is the globular morphology primarily determined by organic factors?
- How large are the pores/channels at the globule walls through which the organic matter is squeezed out? Is the obstruction of these pores/channels responsible for the presence of weakly mineralized globules at sialolith central parts? How large is the pressure build up necessary for the squeezing? Is this a measure of the mineralization driving force?
- Is there flake migration and agglomeration or just precipitation and growth?
- Why are the cores loosely connected to the subsequent layers?
- Do the calcified spheres have the same origin as the globules? Why are they surrounded by a weakly mineralized matrix (Figure 43 (d,e,f))?

The questions raised demonstrate that sialolith investigation is far from exhaustion and that a combined Biology and Materials Science interdisciplinary approach is required for a deeper comprehension of sialolith pathogenesis and etiology.

5 Conclusions

5 Conclusions

The salivary calculi exhibit one core with organic globular structures partially or highly mineralized. The subsequent layers present either laminar or globular structures. These layer types alternate thereafter in succession following a chronologic sequence. Laminar layers consist of fine mineralized strata intercalated with fine organic strata. Globular layers or collars consist of alternating bands of highly calcified globules and bands where globule calcification was still in course. Mineralizing globules are surrounded by teardrop globule crescents also partially mineralized. These structures result from a “squeezing process” induced by pressure buildup and indicate organic matter replacement inside the globules.

The organic matter in the sialoliths contains a high concentration of denaturated collagen, while the mineral matter consists essentially of hydroxyapatite. Mineralization of organic globular structures proceeds by diffusion of Ca and P to the globule interior, followed by precipitation of mineralized flakes, which grow or agglomerate inside the globules and transform during the process into hydroxyapatite.

Higher work of adhesion has been measured in organic globules as compared with calcified regions. Ductile behavior has been detected.

In view of the observations a mechanism for sialolith formation has been proposed based on alternating sedimentary and globular cycles. The globular cycle involves connective tissue invasion followed by calcification of the organic structures.

References

[1] Rauch S, Gorlin RJ. Diseases of the salivary glands. In: Gorlin RJ, Goldman HM, eds. Thoma's Oral Pathology. 6 th ed. St. Louis: Mosby; 1970: 997-1003.

[2] Lustmann J, Regev E, Melamed Y. Sialolithiasis. A survey on 245 patients and a review of the literature. *Int J Oral Maxillofac Surg* 1990; **19** (3): 135-138.

[3] Steiner M, Gould AR, Kushner GM, Weber R, Pesto A. Sialolithiasis of the submandibular gland in 8-year-old child. *Oral Surg, Oral Med, Oral Pathol, Oral Radiol, Endod* 1997; **83**: 188.

[4] Teymoortash A, Wollstein AC, Lippert BM, Peldszus R, Werner JA. Bacteria and Pathogenesis of Human Salivary Calculus. *Acta Otolaryngol* 2002; **122**: 210-214.

[5] Siddiqui SJ. Sialolithiasis: an unusually large submandibular salivary stone. *British Dental Journal* 2002; **193**: 89-91.

[6] Choi J, Kim I-K, Oh N-S. Multiple sialoliths in sublingual gland: Report of a case. *Int J Oral Maxillofac Surg* 2002; **31**: 562-563.

[7] Bilateral multiple sialolithiasis of the parotid gland in a patient with Sjögren's syndrome. *Acta Otorhinolaryngologica Italica* 2007; **27**: 41-44.

[8] Hong KW, Yang YS. Sialolithiasis in the sublingual gland. *Journal of Laryngology & Otology* 2003; **117**: 905-907.

[9] Nahlieli O, Nazarian Y. Sialoendoscopy: A new approach to salivary gland obstructive pathology. *J Am Dent Assoc* 2006; **137** (10): 1394-1400.

[10] Teymoortash A, Buck P, Jepsen H, Werner JA. Sialolith crystals localized intraglandularly and in the Wharton's duct of the human submandibular gland: an X-ray diffraction analysis. *Archives of Oral Biology* 2003; **48**: 233-236.

[11] Grases F, Santiago C, Simonet BM, Costa-Bauzá A. Sialolithiasis: mechanism of calculi formation and etiologic factors. *Clinica Chimica Acta* 2003; **334**: 131-136.

[12] Tanaka N, Ichinose S, Adachi Y, Mimura M, Kimijima Y. Ultrastructural analysis of salivary calculus in combination with X-ray microanalysis. *Med Electron Microsc* 2003; **36**: 120-126.

[13] Kasaboğlu O, Er N, Tümer C, Akkocaoğlu. Micromorphology of Sialoliths in Submandibular Salivary Gland: A Scanning Electron Microscope and X-ray Diffraction Analysis. *J Oral Maxillofac Surg* 2004; **62**: 1253-1258.

[14] Mimura M, Tanaka N, Ichinose S, Kimijima Y, Amagasa T. Possible etiology of calculi formation in salivary glands: biophysical analysis of calculus. *Med Mol Morphol* 2005; **38**: 189-19.

[15] Giray B, Dogan M, Akalin A, Baltrusaitis J, Chan DCN, Skinner HCW, Dogan AU. Sialolith Characterization by Scanning Electron Microscopy and X-ray Photoelectron Spectroscopy. *Scanning* 2007; **29**: 2006-2010.

[16] Alves de Matos AP, Carvalho PA, Almeida A, Duarte L, Vilar R, Leitão J. On the structural diversity of sialoliths. *Microscopy and Microanalysis* 2007; **13** (5): 390-396.

[17] Teymoortash A, Ramaswamy A, Werner JA. Is there evidence of a sphincter system in Wharton's duct? Etiological factors related to sialolith formation. *Jornal of Oral Science* 2003; **45** (4): 233-235.

[18] Takeda Y, Oikawa Y, Satoh M, Nakamura S. Sialolith of the submandibular gland with bone formation. *Pathology International* 2003; **53**: 309-312.

[19] Marchal F, Dulguerov P. Sialolithiasis management: The state of the art. *Arch Otolaryngol Head Neck Surg* 2003; **129** (9): 951-956.

[20] Escudier MP, Brown JE, Drage NA, McGurk M. Extracorporeal shockwave lithotripsy in the management of salivary calculi. *Br J Surg* 2003; **90** (4): 482-485.

[21] Capaccio P, Ottaviani F, Manzo R, et al. Extracorporeal lithotripsy for salivary calculi: A long-term clinical experience. *Laryngoscope* 2004; **114** (6): 1069-1073.

[22] Zenk J, Bozzato A, Winter M, et al. Extracorporeal shock wave lithotripsy of submandibular stones: Evaluation after 10 years. *Ann Otol Rhinol Laryngol* 2004; **113** (5): 378-383.

[23] Baurmash HD. Submandibular salivary stones: Current management modalities. *J Oral Maxillofac Surg* 2004; **62** (3): 369-378.

[24] McGurk M, Escudier MP, Brown JE. Modern management of salivary calculi. *Br J Surg* 2005; **92** (1): 107-112.

[25] Goldstein JI, Newbury DE, Echlin P, Joy DC, Fiori C, Lifshin E, *Scanning Electron Microscopy and X-Ray Microanalysis*, Plenum Press, New York, 1981.

[26] Argon AS, Im J, Safoglu R. Cavity formation from inclusions in ductile fracture. *Metall Trans* 1975; A6: 825.

[27] Gullerud AS, Gao X, Dodds Jr RH, Haj-Ali R.Simulation of ductile crack growth using computational cells: numerical aspects. *Engineering Fracture Mechanics* 2000; **66**: 65-92.

[28] Stuart BH, *Infrared Spectroscopy: Fundamentals and Applications*, Wiley, Chichester, UK, 2005.

[29] Stuart BH*, Biological Applications of Infrared Spectroscopy*, ACOL Series, Wiley, Chichester, UK, 1997.

[30] Chang MC, Tanaka J. FT-IR study for hydroxyapatite/collagen nanocomposite cross-linked by glutaraldehyde. *Biomaterials* 2002; **23**: 4811-4818.

[31] Jastrzebska M, Zalewska-Rejdak J, Mróz I, Barwinsky B, Wrzalik R, Kocot A, Nozynski J. Atomic Force Microscopy and FT-IR Spectroscopy Investigations of Human Heart Valves. *Gen Physiol Bioph* 2006; **25**: 231-244.

[32] Iconomidou VA, Georgaka ME, Chryssikos GD, Gionis V, Megalofonou P, Hamodrakas SJ. Dogfish egg case structural studies by ATR FT-IR and FT-Raman spectroscopy. *Internacional Journal of Biological Macromolecule* 2007; **41:**102-108.

[33] Saitô H, Tabeta R, Shoji A, Ozaki T, Ando I, Miyato T. A High-Resolurion ^{13}C-NMR Study of Collagenlike Polypeptides and Collagen Fibrils in Solid State Studied by the Cross-Polarization-Magic Angle-Spinning Method. Manifestation of Conformation-Dependent ^{13}C Chemical Shifts and Application to Conformational Characterization. *Biopolymers 1984;* **23**: 2279-2297.

[34] Nunes TG, Polido M, Amorim A, Nunes SG, Toledano M. Multinuclear magnetic resonance studies on the chemical interaction of a self-etching adhesive with radicular and coronal human dentin. *J Mater Sci: Mater Med.* 2007; **18**: 2093-2099.

[35] Ando I, Asakura T, *Solid state NMR of polymers*, Elsevier, 1998.

[36] Salerno M, Bykov I. Tutorial: Mapping Adhesion Forces and Calculating Elasticity in Contact-Mode AFM. *Microscopy and Analysis* 2006; **20** (2): S5-S8.

[37] Varkarakis J, Protogerou V, Albanis S, Sofras F, Deliveliotis C. Comparison of success rates and financial cost of extracorporeal shock-wave lithotripsy in situ and after manipulation for proximal ureteral stones. *Urol Res* 2003; **31**: 286–290.

[38] Warpehoski MA, Buscemi PJ, Osborn DC, Finlayson B, Goldberg EP. Distribution of organic matrix in calcium oxalate renal calculi. *Calcified Tissue International* 1981; 33: 211-222.

[39] Grases F, Llobera A. Experimental model to study kidney stones. *Micron* 1998, **29**: 105-111.

[40] Anderson JC, Williams Jr JC, Evan AP, Condon KW, Sommer AJ. Analysis of urinary calculi using an infrared microspectroscopic surface reflectance imaging technique. *Urol Res* 2007; **35**: 211-222.